Comparative Study of Symmetrical Controlled Grid-Connected Inverters

Shuning Gao, *Student Member, IEEE*, Haoran Zhao, *Senior Member, IEEE*, Peng Wang, *Member, IEEE*, Yonghao Gui, *Senior Member, IEEE*, Vladimir Terzija, *Fellow, IEEE*, and Frede Blaabjerg, *Fellow, IEEE*

***Abstract*—The asymmetrical dynamics of the conventional synchronous reference frame phase-locked loop (PLL) enhance the complexity of the system and endanger the stability of the grid-connected voltage source converters. In this article, the admittance modeling of three different symmetrical control strategies, i.e., voltage oriented control with symmetrical PLL, voltage modulated direct power control, and proportional–resonant control, is proposed and uniformed based on the same power tracking property. The voltage feedforward and decoupling of the controllers are both considered. Moreover, due to the symmetrical structure of the three control strategies, their admittance models can directly be modeled under $\alpha\beta$ reference frame as single-input single-output systems. In addition, to reveal the similarity between different control methods and emphasize their differences, the admittance models are constructed by using the same framework. The admittance modeling is verified using frequency-scan, and the control performance is tested using MATLAB/Simulink Simscape Power System and experimental prototype. Finally, the stability criterion based on the proposed admittance modeling is verified by simulation results carried out in real-time simulation platform RTLAB from Opal-RT.**

***Index Terms*—Admittance-based analysis, proportional–resonant (PR) control, voltage modulated (VM) control, voltage oriented control (VOC), voltage source converter (VSC).**

I. Introduction

POWER electronic devices such as voltage source converters (VSCs) have been nowadays widely applied in the modern power system [1]. However, the wideband interactions between the VSC and grid impedance bring potential instability problem to the system and have been brought to the forefront of the academics [2]–[9]. In order to address the challenge, multiple analysis methods have been proposed. Among these methods, the admittance analysis successfully depicts the frequency response of the grid-connected VSC system [10]. Moreover, by equivalenting the system with a Thevenin/Norton equivalent circuit, the admittance-based analysis can easily identify the system stability through the Nyquist stability criterion [4], [6]–[8].

It has been proved that the control strategy of the VSC plays a decisive role in the harmonic interaction between the VSC and power grid [6]. The most typical control strategy of VSC is called voltage oriented control (VOC), which requires a phase-locked loop (PLL) for the grid synchronization [8]. In conventional synchronous reference frame PLL (SRF-PLL), the phase signal of the grid voltage is extracted only by its q-axis component. Therefore, it is inherently asymmetric, which brings a frequency-coupling phenomenon and greatly enhances the complexity of the admittance model [7], [8]. Usually, due to the inherent asymmetrical characteristic, the admittance of the inverter using VOC has to be modeled in the form of a matrix as a multi-input multi-output system [11]. The impedance matrix can be established in the dq reference frame for simplicity. The stability analysis based on dq frame model requires using generalized Nyquist stability criterion [6]. Moreover, the analysis based on dq frame model is not easy to interpret the mechanism of frequency-coupling [12]. The $\alpha\beta$ admittance modeling method based on harmonic linearization is proposed [12], [13]. The $\alpha\beta$ frame admittance modeling approach can readily describe the system in the same coordinate system and, thus, has a more intuitive physical meaning [14], [15]. The neglecting of cross-coupled components in the $\alpha\beta$ modeling leads to inaccuracy of the stability analysis [7]. To describe the generation of coupled components, a complex equivalence method is proposed in [7], which also unifies the dq frame and $\alpha\beta$ frame admittance modeling methods. The coupling is regarded as a conjugate of the corresponding vector under the dq reference frame.

A symmetrical PLL (S-PLL) is proposed in [8]. Compared with SRF-PLL, the S-PLL also tracks the voltage magnitude using a defined imaginary part of the voltage phase signal; thereby, it exhibits symmetrical characteristics and eliminates the generation of frequency-coupling components. The S-PLL based VOC (S-VOC) can also be applied into the doubly fed induction generator for impedance characteristics reshaping and improvement of grid-integration stability [16].

Manuscript received January 25, 2021; revised May 18, 2021 and August 19, 2021; accepted October 2, 2021. Date of publication October 21, 2021; date of current version December 31, 2021. This work was supported by the National Key R&D Program of China under Grant 2018YFA0702200. Recommended for publication by Associate Editor J. Liu. *(Corresponding author: Shuning Gao.)*

Shuning Gao is with the School of Electrical Engineering, Shandong University, Jinan 250061, China, and also with Automation and Control Section, Department of Electronic Systems, Aalborg University, 9220 Aalborg, Denmark (e-mail: gaosn@mail.sdu.edu.cn).

Haoran Zhao and Peng Wang are with the School of Electrical Engineering, Shandong University, Jinan 250061, China (e-mail: hzhao@sdu.edu.cn; wangpengtu@gmail.com).

Yonghao Gui is with Automation and Control Section, Department of Electronic Systems, Aalborg University, 9220 Aalborg, Denmark (e-mail: yg@es.aau.dk).

Vladimir Terzija is with the Skolkovo Institute of Science and Technology, 121205 Moscow, Russia (e-mail: V.Terzija@skoltech.ru).

Frede Blaabjerg is with the Department of Energy Technology, Aalborg University, 9220 Aalborg, Denmark (e-mail: fbl@et.aau.dk).

Color versions of one or more figures in this article are available at https://doi.org/10.1109/TPEL.2021.3122002.

Digital Object Identifier 10.1109/TPEL.2021.3122002

The proportional–resonant (PR) control is also a typical control strategy designed for grid-connected inverters [17]–[21]. Using PR control can reduce the system complexity since it avoids PLL for grid synchronization [21]. It is constructed directly under the $\alpha\beta$ reference frame with a symmetrical structure and can realize zero ac tracking error. However, the control performance cannot be guaranteed once the grid voltage frequency is deviated [18]. A stability assessment of the grid-connected VSC using PR is proposed in [22]. The article focuses on the direct-voltage control, and the power control is not included.

Direct power control (DPC) is also a widely studied VSC control strategy, which successfully avoids the use of PLL [23]–[27]. Conventional lookup table (LUT) based DPC has an nonfixed switching frequency, which deteriorates its steady-state control performance. In recent decades, improved DPC methods such as voltage modulated (VM) DPC and sliding-mode control (SMC) [24] are proposed and widely applied [25]. They obtain constant switching frequency by using space vector modulation (SVM) techniques and thus have better steady-state performance compared to the conventional DPC methods. The VM-DPC is recently proved to be effective and widely applicable [26], [28], [29]. It improves the performance of VSC compared with SMC and LUT-DPC. In addition, the VM-DPC maintains a satisfactory steady-state performance similar to that of conventional VOC [25]. The VM-DPC is a symmetrical control method, and its admittance model can be linearized and built directly under $\alpha\beta$ frame [30]. Note that the VM-DPC still brings frequency coupling phenomenon due to the inherent power integration. However, the coupling can be restrained by using a bandpass filter (BPF).

Note that it is normally difficult to compare the admittance characteristics of different control methods fairly partly because the control parameters are always selected based on a specific control structure to meet the best performance, i.e., the best input reference tracking property. Therefore, one of the purposes of this article is to unify the power tracking properties of three different symmetrical controllers, i.e., S-VOC, PR control, and VM-DPC. Among three control methods, S-VOC and PR are both typical linear control methods, and the VM-DPC is a DPC method using SVM. Then, based on the same power tracking property, the admittance characteristics of the three control strategies are presented and compared in detail. The innovations can be summarized as follows.

1) The power tracking properties of three different symmetrical control methods are described by using a unified second-order transfer function. The unified control performance of three controllers is verified using simulation carried out in MATLAB/Simulink Simscape electrical and experimental prototype.
2) The admittance models of three symmetrical controllers are summarized. To further reveal interconnection and the difference between the three control methods, the proposed admittances are presented as a unified basic admittance plus additional virtual admittance determined by different controllers. The admittances are modeled directly under the $\alpha\beta$ reference frame with a clear physical meaning.

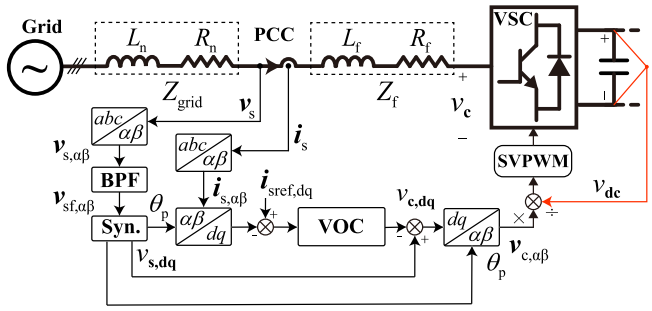

Fig. 1. Diagram of grid-connected voltage source converter (VSC) using voltage oriented control (VOC).

3) The effects of the three symmetrical control structures on the harmonic response and stability of grid-connected inverters are compared. The accuracy of the Nyquist stability analysis based on the proposed admittance modeling method is verified using real-time simulation platform RTLAB from Opal-RT.

The rest of this article is organized as follows. An overview of the admittance analysis of VSC using conventional VOC and frequency-coupling phenomenon caused by SRF-PLL is discussed in Section II. The admittance modeling of three different symmetrical control strategies is presented in Section III. A unified performance analysis is presented in Section IV. In Section V, the admittance modeling methods of three symmetrical controllers are presented. Section VI presents the simulation results. Finally, Section VI concludes this article.

II. Overview of Admittance Analysis of VOC-Based Grid-Connected Inverters

To better introduce the concept of symmetrical control, an overview of the admittance analysis of the conventional VOC is introduced. Moreover, the frequency-coupling phenomenon caused by SRF-PLL is explained using the $\alpha\beta$ frame admittance model. This article focuses on the inner loop dynamics, and the dc voltage is considered to be constant. Moreover, the dynamics of pulsewidth modulation (PWM) are neglected in the admittance modeling. The modulation is considered to be capable of generating output as an ideal voltage waveform.

A. Voltage Oriented Control of VSC

A typical grid-connected VSC is presented in Fig. 1, where the complex space vectors of the voltage and current can be denoted by the sum of their fundamental components and harmonic components using boldface letters, e.g., $\boldsymbol{v}_s = \boldsymbol{v}_{s1} + \tilde{\boldsymbol{v}}_{sh}$, $\boldsymbol{i}_s = \boldsymbol{i}_{s1} + \tilde{\boldsymbol{i}}_{sh}$. Take the point of common coupling (PCC) voltage $\boldsymbol{v}_s$ as an example, and the space vector can either be presented under $\alpha\beta$ or under dq frame as follows:

$$\boldsymbol{v}_s = \underbrace{v_{s1,\alpha} + jv_{s1,\beta}}_{\boldsymbol{v}_{s1,\alpha\beta}} + \underbrace{\tilde{v}_{sh,\alpha} + j\tilde{v}_{sh,\beta}}_{\tilde{\boldsymbol{v}}_{sh,\alpha\beta}}$$

$$\boldsymbol{v}_s = \underbrace{v_{s1,d} + jv_{s1,q}}_{\boldsymbol{v}_{s1,dq}} + \underbrace{\tilde{v}_{sh,d} + j\tilde{v}_{sh,q}}_{\tilde{\boldsymbol{v}}_{sh,dq}}. \quad (1)$$

The basic equation of the grid-connected VSC is

$$\boldsymbol{v}_{\rm s}-\boldsymbol{v}_{\rm c}=R_{\rm f}\boldsymbol{i}_{\rm s}+L_{\rm f}\frac{d\boldsymbol{i}_{\rm s}}{dt} \tag{2}$$

where $\boldsymbol{v}_{\rm c}$ and $\boldsymbol{i}_{\rm s}$ are the VSC voltage and output current, and $R_{\rm f}$ and $L_{\rm f}$ are the resistance and inductance of VSC filter. Using (2), the fundamental components of the grid-connected VSC can be also written in s' domain under dq frame as follows:

$$\boldsymbol{v}_{\rm s1,dq}-\boldsymbol{v}_{\rm c1,dq}=[R_{\rm f}+(s'+j\omega_{\rm s})L_{\rm f}]\boldsymbol{i}_{\rm s1,dq} \tag{3}$$

where $\boldsymbol{v}_{\rm c1,dq}$ and $\boldsymbol{i}_{\rm s1,dq}$ are the fundamental space vectors of the VSC voltage and the current under dq frame, respectively. $\omega_{\rm s}$ denotes the fundamental frequency of the grid voltage. The relation can be translated into the stationary reference frame using $s=s'+j\omega_{\rm s}$, and the equation of the harmonic components can be expressed in $\alpha\beta$ frame as follows:

$$\tilde{\boldsymbol{v}}_{{\rm sh},\alpha\beta}-\tilde{\boldsymbol{v}}_{{\rm ch},\alpha\beta}=(R_{\rm f}+sL_{\rm f})\tilde{\boldsymbol{i}}_{{\rm sh},\alpha\beta} \tag{4}$$

where $\tilde{\boldsymbol{v}}_{{\rm ch},\alpha\beta}$ and $\tilde{\boldsymbol{i}}_{{\rm sh},\alpha\beta}$ denote the harmonic components of $\boldsymbol{v}_{{\rm c},\alpha\beta}$ and $\boldsymbol{i}_{{\rm s},\alpha\beta}$, respectively. The filter admittance is denoted by $Y_{\rm f}=1/Z_{\rm f}(s)=1/(R_{\rm f}+sL_{\rm f})$.

The voltage harmonics $\boldsymbol{v}_{\rm sh}$ at the PCC may deteriorate the performance of the PLL and VSC controller. Therefore, a BPF is utilized in this article to block the harmonics and dc components in the measured PCC voltage. The transfer function of the BPF can be expressed in the $\alpha\beta$ frame as follows:

$$G_{\rm fil}(s)=\frac{2\omega_{\rm c}s}{s^2+2\omega_{\rm c}s+\omega_{\rm s}^2} \tag{5}$$

where $\omega_{\rm c}=\zeta_{\rm f}\omega_{\rm s}$ is the resonance bandwidth of the BPF, and $\zeta_{\rm f}$ is the damping ratio of the BPF. Note that $G_{\rm fil}(j\omega_{\rm s})=1$. Therefore, the voltage input of the controller can be expressed under $\alpha\beta$ and dq reference frames, respectively, as follows:

$$\begin{aligned}\boldsymbol{v}_{{\rm sf},\alpha\beta}&=\boldsymbol{v}_{{\rm s1},\alpha\beta}+\underbrace{G_{\rm fil}(s)\tilde{\boldsymbol{v}}_{{\rm sh},\alpha\beta}}_{\tilde{\boldsymbol{v}}_{{\rm shf},\alpha\beta}}\\ \boldsymbol{v}_{\rm sf,dq}&=\boldsymbol{v}_{\rm s1,dq}+\underbrace{G_{\rm fil}(s'+j\omega_{\rm s})\tilde{\boldsymbol{v}}_{\rm sh,dq}}_{\tilde{\boldsymbol{v}}_{\rm shf,dq}}\end{aligned} \tag{6}$$

where $\tilde{\boldsymbol{v}}_{{\rm shf},\alpha\beta}$ and $\tilde{\boldsymbol{v}}_{\rm shf,dq}$ denote the filtered voltage input under $\alpha\beta$ and dq reference frames, respectively. Note that the most typical control used in practical VSC is the symmetrically decoupled PI control consisting of current feedforward decoupling and voltage feedforward linearization components. Therefore, the fundamental component of the VSC voltage $\boldsymbol{v}_{\rm c1,dq}$ can be expressed in terms of the fundamental components in the dq reference frame as follows:

$$\begin{aligned}\boldsymbol{v}_{\rm c1,dq}=&-\underbrace{L_{\rm f}\left(K_{\rm p}+\frac{K_{\rm i}}{s'}\right)}_{G_{\rm PI,dq}(s')}(\boldsymbol{i}_{\rm sref,dq}-\boldsymbol{i}_{\rm s1,dq})\\ &\underbrace{-j\omega_{\rm s}L_{\rm f}i_{\rm s1,dq}+\boldsymbol{v}_{\rm s1,dq}}_{\text{current/voltage feedforward}}\end{aligned} \tag{7}$$

where $G_{\rm PI,dq}(s')$ denotes the basic PI control unit, and $K_{\rm p}$ and $K_{\rm i}$ are the PI control parameters. The current references $\boldsymbol{i}_{\rm sref,dq}$ and the current fundamental component $i_{\rm s1,dq}$ can be calculated as follows:

$$\boldsymbol{i}_{\rm sref,dq}=-\frac{2}{3}\frac{\boldsymbol{S}_{\rm sref}}{|v_{\rm s1}|}\,\boldsymbol{i}_{\rm s1,dq}=-\frac{2}{3}\frac{\boldsymbol{S}_{\rm s1}}{|v_{\rm s1}|} \tag{8}$$

where $S_{\rm sref}=P_{\rm sref}+jQ_{\rm sref}$ denotes the reference of output complex power. $S_{\rm s1}=P_{\rm s1}+jQ_{\rm s1}=-\frac{3}{2}[{\rm Re}(\boldsymbol{v}_{\rm s1}\boldsymbol{i}_{\rm s1}^*)+j{\rm Im}(\boldsymbol{v}_{\rm s1}\boldsymbol{i}_{\rm s1}^*)]$ represents the fundamental components of the instantaneous complex power. By neglecting the harmonic components and the dynamics of time delay, the power tracking dynamics can be described as a second-order transfer function by substituting (6) and (7) into (3)

$$T_{\rm VSC}^{\rm PI}=\frac{\boldsymbol{i}_{\rm s1,dq}}{\boldsymbol{i}_{\rm sref,dq}}=\frac{\boldsymbol{S}_{\rm s1,dq}}{\boldsymbol{S}_{\rm sref,dq}}=\frac{K_{\rm p}s'+K_{\rm i}}{s'^2+(K_{\rm p}+\frac{R_{\rm f}}{L_{\rm f}})s'+K_{\rm i}}. \tag{9}$$

To ensure the performance of fundamental dc regulation, normally, the control parameters can be chosen based on the natural frequency $\omega_{\rm n}$ and damping factor ζ derived from the characteristic polynomial of (9) [31]

$$\begin{cases}K_{\rm i}=\omega_{\rm n}^2\\ K_{\rm p}=2\zeta_{\rm n}\omega_{\rm n}-\frac{R_{\rm f}}{L_{\rm f}}\end{cases}. \tag{10}$$

Except for the fundamental components, the voltage output is also affected by the current and voltage harmonics as follows:

$$\tilde{\boldsymbol{v}}_{\rm ch,dq}=G_{\rm del}(s)[\underbrace{(L_{\rm f}G_{\rm PI,dq}(s')-j\omega_{\rm s}L_{\rm f})}_{{\rm G_{c,dq}(s')}}\tilde{\boldsymbol{i}}_{\rm sh,dq}+\tilde{\boldsymbol{v}}_{\rm shf,dq}] \tag{11}$$

where $G_{\rm c,dq}(s')$ denotes the influence of PI control with feedforward on VSC voltage harmonics. Note that the time delay dynamics represented by $G_{\rm del}(s)$ is [7], [22]

$$G_{\rm del}(s)=e^{-1.5T_{\rm del}s}\approx\frac{1-1.5T_{\rm del}s}{1+1.5T_{\rm del}s} \tag{12}$$

where $T_{\rm del}$ is the sampling period. Using the frequency translation $s'=s-j\omega_{\rm s}$, $\tilde{\boldsymbol{v}}_{\rm ch,dq}$ can also be written under the $\alpha\beta$ frame as follows:

$$\begin{aligned}\tilde{\boldsymbol{v}}_{{\rm ch},\alpha\beta}=G_{\rm del}(s)[&\underbrace{(L_{\rm f}G_{{\rm PI},\alpha\beta}(s-j\omega_{\rm s})-j\omega_{\rm s}L_{\rm f})}_{{\rm G_{c,\alpha\beta}(s-j\omega_s)}}\tilde{\boldsymbol{i}}_{{\rm sh},\alpha\beta}\\ &+\tilde{\boldsymbol{v}}_{{\rm shf},\alpha\beta}].\end{aligned} \tag{13}$$

The admittance of VSC with the PI control, denoting its harmonic-domain response, can be derived in the $\alpha\beta$ reference frame by substituting (6) and (13) into (4) as follows:

$$Y_{\rm VSC}^{\rm PI}=\frac{\tilde{\boldsymbol{i}}_{{\rm sh},\alpha\beta}}{\tilde{\boldsymbol{v}}_{{\rm sh},\alpha\beta}}=\frac{Y_{\rm f}(s)[1-G_{\rm del}(s)G_{\rm fil}(s)]}{1+G_{\rm del}(s)Y_{\rm f}(s)G_{{\rm c},\alpha\beta}(s-j\omega_{\rm s})}. \tag{14}$$

Note that $T_{\rm VSC}^{\rm PI}$ and $Y_{\rm VSC}^{\rm PI}$ represent the power tracking property and the response to the voltage harmonics, respectively. $Y_{\rm VSC}^{\rm PI}$ mainly affects the small-signal stability of the grid-connected VSC under weak-grid conditions. Moreover, it can be found that $Y_{\rm VSC}^{\rm PI}$ is only related to the control parameters and has no relation with the system operation point.

B. SRF-PLL and Frequency Coupling Phenomenon

Recent studies revealed that the SRF-PLL affects the harmonic response of the system and introduced frequency coupling phenomenon due to its asymmetrical structure. For the modeling of SRF-PLL, an $\alpha\beta$ frame admittance modeling presented in [7] is used in this section. The input of the PLL is a filtered PCC voltage $\boldsymbol{v}^{\mathrm{s}}_{\mathrm{sf},\alpha\beta}$ under the $\alpha\beta$ reference frame, and the dq-transformation using SRF-PLL can be decomposed as follows:

$$\begin{aligned}\boldsymbol{v}^{\mathrm{c}}_{\mathrm{sf,dq}} &= \boldsymbol{v}^{\mathrm{s}}_{\mathrm{sf},\alpha\beta}e^{-j\theta_{\mathrm{p}}} \\ &= \boldsymbol{v}^{\mathrm{s}}_{\mathrm{sf,dq}}e^{-j\Delta\theta_{\mathrm{PLL}}} = (\boldsymbol{v}^{\mathrm{s}}_{\mathrm{s1,dq}} + \tilde{\boldsymbol{v}}^{\mathrm{s}}_{\mathrm{shf,dq}})e^{-j\Delta\theta_{\mathrm{PLL}}} \\ &\approx (\boldsymbol{v}^{\mathrm{s}}_{\mathrm{s1,dq}} + \tilde{\boldsymbol{v}}^{\mathrm{s}}_{\mathrm{shf,dq}})(1 - j\Delta\theta_{\mathrm{PLL}}) \\ &= \boldsymbol{v}^{\mathrm{s}}_{\mathrm{s1,dq}} + \underbrace{\tilde{\boldsymbol{v}}^{\mathrm{s}}_{\mathrm{shf,dq}} - j\boldsymbol{v}^{\mathrm{s}}_{\mathrm{s1,dq}}\Delta\theta_{\mathrm{PLL}}}_{\tilde{\boldsymbol{v}}^{\mathrm{VOC}}_{\mathrm{spf,dq}}} - \underbrace{j\tilde{\boldsymbol{v}}^{\mathrm{s}}_{\mathrm{shf,dq}}\Delta\theta_{\mathrm{PLL}}}_{\text{Negligible}}\end{aligned} \tag{15}$$

where the superscripts $'s'$ and $'c'$ denote the grid dq reference frame and PLL dq reference frame, respectively. $\theta_{\mathrm{p}} = \omega_s t + \Delta\theta_{\mathrm{PLL}}$ is the detected voltage phase angle. Note that $\boldsymbol{v}^{\mathrm{s}}_{\mathrm{s1,dq}}$ represents the fundamental components of the voltage, under the dq reference frame, $\boldsymbol{v}^{\mathrm{s}}_{\mathrm{s1,dq}} = |\boldsymbol{v}_{\mathrm{s1}}|$. The effect of the PLL tracking error to the harmonic components is very small; thus, it can be neglected, i.e., $\tilde{\boldsymbol{v}}^{\mathrm{s}}_{\mathrm{shf,dq}} \approx \tilde{\boldsymbol{v}}^{\mathrm{c}}_{\mathrm{shf,dq}}$. Therefore, the superscripts $'c'$ and $'s'$ are ignored in the following. $\Delta\theta_{\mathrm{PLL}}$ is the error between the detected voltage phase and actual grid voltage phase value. $\tilde{\boldsymbol{v}}_{\mathrm{shf,dq}}\Delta\theta_{\mathrm{PLL}}$ denotes the coupling between voltage harmonics and the error of phase measurement, which is small enough to be neglected. The total variation of the measured voltage can be defined as $\tilde{\boldsymbol{v}}^{\mathrm{VOC}}_{\mathrm{spf,dq}}$. Note that $\tilde{\boldsymbol{v}}^{\mathrm{VOC}}_{\mathrm{spf,dq}}$ can be separately presented by its d- and q-axis components as follows:

$$\begin{cases}\tilde{v}^{\mathrm{VOC}}_{\mathrm{spf,d}} = \tilde{v}_{\mathrm{shf,d}} \\ \tilde{v}^{\mathrm{VOC}}_{\mathrm{spf,q}} = \tilde{v}_{\mathrm{shf,q}} - |\boldsymbol{v}_{\mathrm{s1}}|\Delta\theta_{\mathrm{PLL}}.\end{cases} \tag{16}$$

The SRF-PLL is designed based on the variation of the q-axis voltage component $\tilde{v}^{\mathrm{VOC}}_{\mathrm{spf,q}}$

$$\Delta\theta_{\mathrm{PLL}} = \frac{1}{s'}\underbrace{\left(K_{\mathrm{PLL,p}} + \frac{K_{\mathrm{PLL,i}}}{s'}\right)}_{H_{\mathrm{PLL}}(s')}\tilde{v}^{\mathrm{VOC}}_{\mathrm{spf,q}} \tag{17}$$

where $K_{\mathrm{PLL,p}}$ and $K_{\mathrm{PLL,i}}$ denote the parameters of SRF-PLL. By substituting (17) into (16), the following is obtained:

$$\Delta\theta_{\mathrm{PLL}} = \underbrace{\frac{H_{\mathrm{PLL}}(s')}{s' + |\boldsymbol{v}_{\mathrm{s1}}|H_{\mathrm{PLL}}(s')}}_{T_{\mathrm{PLL}}(s')}\tilde{v}_{\mathrm{shf,q}}. \tag{18}$$

The small-signal block diagram of the conventional SRF-PLL is shown in Fig. 2. Note that the main reason of the frequency-coupling caused by SRF-PLL is its inherent unsymmetrical structure. The one-dimensional voltage input under q-axis $v_{\mathrm{shf,q}}$ can be seen as the sum of two conjugated vectors, i.e., $\tilde{\boldsymbol{v}}_{\mathrm{shf,dq}}$ and $\tilde{\boldsymbol{v}}^{*}_{\mathrm{shf,dq}}$ [7], [8]. Therefore, the phase variation $\Delta\theta_{\mathrm{PLL}}$ can

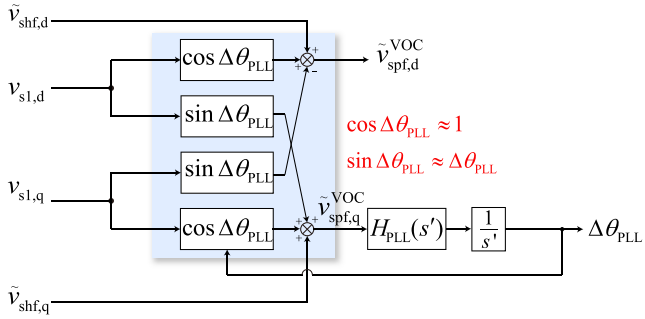

Fig. 2. Small-signal block diagram of the conventional single-reference frame phase-locked loop (SRF-PLL).

be expressed as follows:

$$\Delta\theta_{\mathrm{PLL}} = T_{\mathrm{PLL}}(s')\frac{\tilde{\boldsymbol{v}}_{\mathrm{shf,dq}} - \tilde{\boldsymbol{v}}^{*}_{\mathrm{shf,dq}}}{2j}. \tag{19}$$

Based on the derivation similar to (15), the current harmonic components of the control signal are depicted as follows:

$$\tilde{\boldsymbol{i}}^{\mathrm{VOC}}_{\mathrm{sp,dq}} = \tilde{\boldsymbol{i}}_{\mathrm{sh,dq}} - j\boldsymbol{i}_{\mathrm{s1,dq}}\Delta\theta_{\mathrm{PLL}}. \tag{20}$$

The controlled VSC voltage is also affected by the PLL during the inversion dq transform, which can be derived as

$$\tilde{\boldsymbol{v}}^{\mathrm{VOC}}_{\mathrm{ch,dq}} = \tilde{\boldsymbol{v}}_{\mathrm{cp,dq}} + j\boldsymbol{v}_{\mathrm{c1,dq}}\Delta\theta_{\mathrm{PLL}}. \tag{21}$$

Therefore, the harmonics of the components can be derived by substituting (19) into (15), (20), and (21) and given as

$$\begin{aligned}\tilde{\boldsymbol{v}}^{\mathrm{VOC}}_{\mathrm{spf,dq}} &= \tilde{\boldsymbol{v}}_{\mathrm{shf,dq}} - \underbrace{T_{\mathrm{PLL}}(s')\boldsymbol{v}_{\mathrm{s1,dq}}}_{G_{\mathrm{vs,pll}}(s')}\frac{\tilde{\boldsymbol{v}}_{\mathrm{shf,dq}} - \tilde{\boldsymbol{v}}^{*}_{\mathrm{shf,dq}}}{2} \\ \tilde{\boldsymbol{i}}^{\mathrm{VOC}}_{\mathrm{sp,dq}} &= \tilde{\boldsymbol{i}}_{\mathrm{sh,dq}} - \underbrace{T_{\mathrm{PLL}}(s')\boldsymbol{i}_{\mathrm{s1,dq}}}_{G_{\mathrm{is,pll}}(s')}\frac{\tilde{\boldsymbol{v}}_{\mathrm{shf,dq}} - \tilde{\boldsymbol{v}}^{*}_{\mathrm{shf,dq}}}{2} \\ \tilde{\boldsymbol{v}}^{\mathrm{VOC}}_{\mathrm{ch,dq}} &= G_{\mathrm{del}}(s)\left[\tilde{\boldsymbol{v}}^{\mathrm{VOC}}_{\mathrm{cp,dq}} + \underbrace{T_{\mathrm{PLL}}(s')\tilde{\boldsymbol{v}}_{\mathrm{c1,dq}}}_{G_{\mathrm{vc,pll}}(s')}\frac{\tilde{\boldsymbol{v}}_{\mathrm{shf,dq}} - \tilde{\boldsymbol{v}}^{*}_{\mathrm{shf,dq}}}{2}\right]\end{aligned} \tag{22}$$

where $G_{\mathrm{is,pll}}(s')$ denotes the effect of asymmetrical SRF-PLL on the current inputs. $G_{\mathrm{vc,pll}}(s')$ represents the influence of the SRF-PLL on the dq inverse transformation of the VSC output voltage and $G_{\mathrm{vs,pll}}(s')$ expresses the effect of the SRF-PLL on voltage feedforward components. For simplicity, the harmonics of the VSC voltage are considered to be equal to the output signal $\boldsymbol{v}^{\mathrm{PLL}}_{\mathrm{ch,dq}}$. Therefore, the effect of VOC and PLL on the control can be expressed as

$$\begin{aligned}\tilde{\boldsymbol{v}}^{\mathrm{VOC}}_{\mathrm{ch,dq}} = G_{\mathrm{del}}(s)\Bigg[&G_{\mathrm{c,dq}}(s')\tilde{\boldsymbol{i}}^{\mathrm{VOC}}_{\mathrm{sp,dq}} + \tilde{\boldsymbol{v}}^{\mathrm{VOC}}_{\mathrm{spf,dq}} \\ &+ G_{\mathrm{vc,pll}}(s')\frac{\tilde{\boldsymbol{v}}_{\mathrm{shf,dq}} - \tilde{\boldsymbol{v}}^{*}_{\mathrm{shf,dq}}}{2}\Bigg].\end{aligned} \tag{23}$$

The small-signal block diagram of the conventional VOC is shown in Fig. 3. Furthermore, (23) can be simplified as follows:

$$\tilde{\boldsymbol{v}}^{\mathrm{VOC}}_{\mathrm{ch,dq}} = \tilde{\boldsymbol{v}}^{\mathrm{VOC}}_{\mathrm{ch1,dq}} + \tilde{\boldsymbol{v}}^{\mathrm{VOC}}_{\mathrm{ch2,dq}} \tag{24}$$

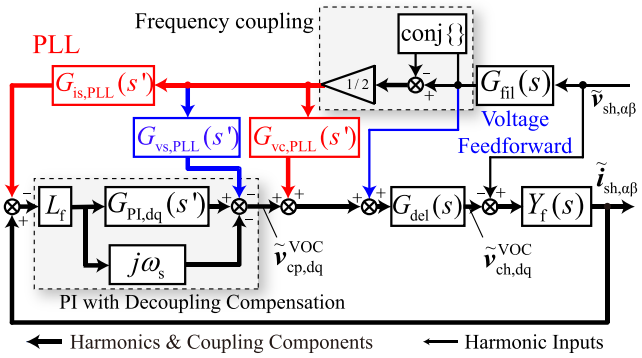

Fig. 3. Small-signal block diagram of grid-connected voltage source converter using SRF-PLL based VOC.

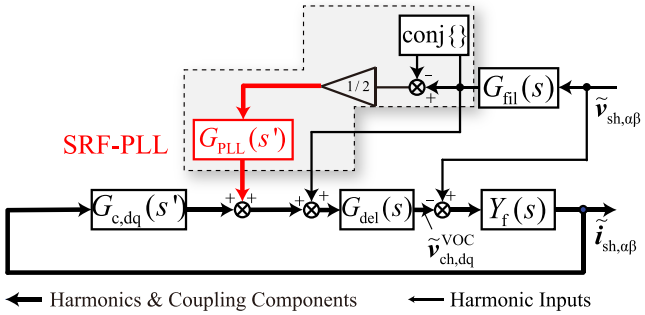

Fig. 4. Simplified small-signal block diagram of grid-connected voltage source converter using SRF-PLL based VOC.

where $\tilde{\boldsymbol{v}}^{\mathrm{VOC}}_{\mathrm{ch1,dq}}$ and $\tilde{\boldsymbol{v}}^{\mathrm{VOC}}_{\mathrm{ch2,dq}}$ denote the positive-sequence components and coupling components of the controlled VSC voltage separately

$$\begin{cases} \tilde{\boldsymbol{v}}^{\mathrm{VOC}}_{\mathrm{ch1,dq}} = G_{\mathrm{del}}(s)\Big(G_{\mathrm{c,dq}}(s')\tilde{\boldsymbol{i}}_{\mathrm{sh,dq}} \\ \qquad\qquad +\tilde{\boldsymbol{v}}_{\mathrm{shf,dq}} + \frac{1}{2}G_{\mathrm{PLL}}(s')\tilde{\boldsymbol{v}}_{\mathrm{shf,dq}}\Big) \\ \tilde{\boldsymbol{v}}^{\mathrm{VOC}}_{\mathrm{ch2,dq}} = \frac{1}{2}G_{\mathrm{del}}(s)G_{\mathrm{PLL}}(s')\tilde{\boldsymbol{v}}^{*}_{\mathrm{shf,dq}} \end{cases} \tag{25}$$

where $G_{\mathrm{PLL}}(s')$ denotes the effect of PLL on the system harmonic response

$$G_{\mathrm{PLL}}(s') = -G_{\mathrm{c,dq}}(s')G_{\mathrm{is,pll}}(s') - G_{\mathrm{vs,pll}}(s') + G_{\mathrm{vc,pll}}(s'). \tag{26}$$

Using (24), the small-signal block diagram of VOC can be simplified as shown in Fig. 4. Due to the frequency-coupling effect caused by the SRF-PLL, the harmonics disturbance v_{sh} at PCC generates two components with different frequencies, i.e., $\tilde{\boldsymbol{v}}^{\mathrm{VOC}}_{\mathrm{ch1,dq}}$ at $\omega_{\mathrm{s}}-\omega_{\mathrm{h}}$ and $\tilde{\boldsymbol{v}}^{\mathrm{VOC}}_{\mathrm{ch2,dq}}$ at $\omega_{\mathrm{h}}-\omega_{\mathrm{s}}$, in the VSC output voltage. The generation process of the current coupling-component $\tilde{\boldsymbol{i}}_{\mathrm{sh2,dq}}$ under dq reference frame, i.e., the coupling components under $\alpha\beta$ reference frame $\tilde{\boldsymbol{i}}_{\mathrm{sh2},\alpha\beta}$ with frequency $2\omega_{\mathrm{s}}-\omega_{\mathrm{h}}$ can be summarized as follows:

$$\begin{aligned} &\tilde{\boldsymbol{v}}^{\mathrm{VOC}}_{\mathrm{ch1,dq}}|_{\omega_h-\omega_s} \rightarrow \tilde{\boldsymbol{i}}_{\mathrm{sh1},\alpha\beta}|_{\omega_h} \\ \tilde{\boldsymbol{v}}_{\mathrm{sh},\alpha\beta} \rightarrow \tilde{\boldsymbol{v}}_{\mathrm{sh,dq}}\langle &\tilde{\boldsymbol{v}}^{\mathrm{VOC}}_{\mathrm{ch2,dq}}|_{\omega_s-\omega_h} \rightarrow \tilde{\boldsymbol{i}}_{\mathrm{sh2},\alpha\beta}|_{2\omega_s-\omega_h}. \end{aligned} \tag{27}$$

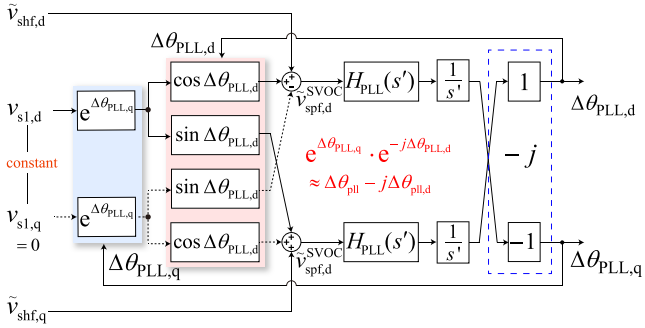

Fig. 5. Small-signal block diagram of the symmetrical phase-locked loop (PLL).

III. Symmetrical Control

In this section, the three different symmetrical control methods, i.e., S-VOC, VM-DPC, and PR, are introduced and compared.

A. VOC Using Symmetrical PLL (S-VOC)

The unsymmetrical PLL can be transformed into a symmetrical one by replacing the original phase angle with a complex one $\boldsymbol{\theta} = \theta_{\mathrm{d}} + j\theta_{\mathrm{q}}$ [8]. Using the complex phase angle and the approximation similar to (15), the dq-transformation carried out by the symmetrical PLL can be expressed as

$$\begin{aligned} \boldsymbol{v}_{\mathrm{s,dq}} &= (|\boldsymbol{v}_{\mathrm{s1}}| + \tilde{\boldsymbol{v}}_{\mathrm{shf,dq}})e^{-j\Delta\boldsymbol{\theta}_{\mathrm{PLL}}} \\ &\approx (|\boldsymbol{v}_{\mathrm{s1}}| + \underbrace{\tilde{\boldsymbol{v}}_{\mathrm{shf,dq}} - |\boldsymbol{v}_{\mathrm{s1}}|\Delta\boldsymbol{\theta}_{\mathrm{PLL}}}_{\tilde{\boldsymbol{v}}^{\mathrm{SVOC}}_{\mathrm{spf,dq}}}) \end{aligned} \tag{28}$$

where the phase and magnitude oscillation caused by the voltage harmonics can be approximated as $e^{-j\Delta\boldsymbol{\theta}_{\mathrm{PLL}}} \approx \Delta\theta_{\mathrm{PLL,q}} - j\Delta\theta_{\mathrm{PLL,d}}$. $\Delta\theta_{\mathrm{PLL,d}}$ represents the phase tracking error. The additional $\Delta\theta_{\mathrm{PLL,q}}$ denotes the voltage magnitude oscillation caused by the harmonics. Therefore, the disturbance of the measured voltage signal $\tilde{\boldsymbol{v}}^{\mathrm{SVOC}}_{\mathrm{spf,dq}}$ in the symmetrical PLL can be expressed as

$$\begin{cases} \tilde{v}^{\mathrm{SVOC}}_{\mathrm{spf,d}} = \tilde{v}_{\mathrm{shf,d}} - |\boldsymbol{v}_{\mathrm{s1}}|\Delta\theta_{\mathrm{PLL,q}} \\ \tilde{v}^{\mathrm{SVOC}}_{\mathrm{spf,q}} = \tilde{v}_{\mathrm{shf,q}} - |\boldsymbol{v}_{\mathrm{s1}}|\Delta\theta_{\mathrm{PLL,d}}. \end{cases} \tag{29}$$

Compared with (16), it shows that the error of the voltage magnitude $\tilde{v}^{\mathrm{SVOC}}_{\mathrm{spf,d}}$ is also tracked by $\Delta\theta_{\mathrm{PLL,q}}$. The structure is overall a symmetrical one. Therefore, using the definition of $\boldsymbol{\Delta\theta}_{\mathrm{PLL}}$, the symmetrical PLL is designed as

$$\boldsymbol{\Delta\theta}_{\mathrm{PLL}} = -j\frac{1}{s'}H_{\mathrm{PLL}}(s')\tilde{\boldsymbol{v}}^{\mathrm{SVOC}}_{\mathrm{spf,dq}}. \tag{30}$$

The equivalent small-signal model of the symmetrical PLL is shown in Fig. 5. Substituting (30) into (29) yields

$$\boldsymbol{\Delta\theta}_{\mathrm{PLL}} = -jT_{\mathrm{PLL}}(s')\tilde{\boldsymbol{v}}_{\mathrm{shf,dq}}. \tag{31}$$

Compared with (19), the conjugate part $\tilde{\boldsymbol{v}}^{*}_{\mathrm{shf,dq}}$ is eliminated. Therefore, the output VSC voltage signal can be simplified as

$$\begin{aligned} \tilde{\boldsymbol{v}}^{\mathrm{SVOC}}_{\mathrm{ch,dq}} &= G_{\mathrm{del}}(s)G_{\mathrm{c,dq}}(s')\tilde{\boldsymbol{i}}_{\mathrm{sh,dq}} \\ &\quad + G_{\mathrm{del}}(s)G_{\mathrm{fil}}(s)[1 + G_{\mathrm{PLL}}(s')]\tilde{\boldsymbol{v}}_{\mathrm{sh,dq}}. \end{aligned} \tag{32}$$

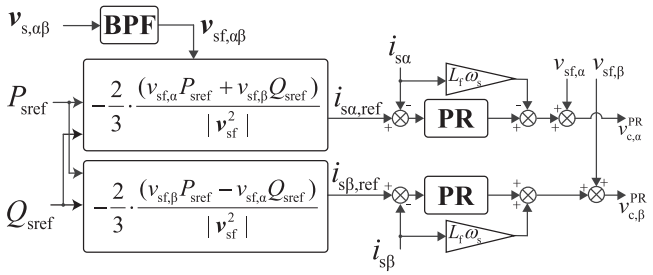

Fig. 6. Block diagram of PR control.

Similar to (13), the expression of (32) in the $\alpha\beta$ frame can be found by replacing s' with $s - j\omega_{\rm s}$ given as

$$\tilde{\boldsymbol{v}}^{\rm SVOC}_{{\rm ch},\alpha\beta} = G_{\rm del}(s)G_{{\rm c},\alpha\beta}(s-j\omega_{\rm s})\tilde{\boldsymbol{i}}_{{\rm sh},\alpha\beta} + G_{\rm del}(s)G_{\rm fil}(s)[1+G_{\rm PLL}(s-j\omega_{\rm s})]\tilde{\boldsymbol{v}}_{{\rm sh},\alpha\beta}. \tag{33}$$

Since the harmonic admittance of VSC using symmetrical PLL can be expressed as a single-input single-output (SISO) system, based on the basic admittance $Y^{\rm PIs}_{\rm VSC}$, the equivalent admittance of the grid-connected VSC using symmetrical PLL-based VOC can be deduced by substituting (32) into (3) as follows:

$$\boldsymbol{Y}^{\rm SVOC}_{\rm VSC} = \frac{\tilde{\boldsymbol{i}}_{{\rm sh},\alpha\beta}}{\tilde{\boldsymbol{v}}_{{\rm sh},\alpha\beta}} = Y^{\rm PI}_{\rm VSC} + Y^{\rm SVOC}_{\rm n} \tag{34}$$

where $Y^{\rm SVOC}_{\rm n}$ denotes the additional virtual admittance of the symmetrical PLL on the original $Y^{\rm PI}_{\rm VSC}$. The expression of $Y^{\rm SVOC}_{\rm n}$ is

$$Y^{\rm SVOC}_{\rm n} = [1+Y_{\rm f}(s)G_{{\rm c},\alpha\beta}(s-j\omega_{\rm s})]^{-1}Y_{\rm f}(s) \cdot G_{\rm fil}(s)G_{\rm PLL}(s-j\omega_{\rm s}) \quad . \tag{35}$$

Note that the value of the voltage magnitude $|v_{\rm s1}|$ in symmetrical PLL should be updated in real time according to the system operation point.

B. PR Control

The basic control structure of a PR control is shown in Fig. 6. The outer loop can be written in terms of complex vectors as

$$\boldsymbol{i}_{{\rm sref},\alpha\beta} = -\frac{2}{3}\frac{1}{|\boldsymbol{v}^2_{\rm sf}|}\boldsymbol{v}_{{\rm sf},\alpha\beta}(P_{\rm sref} - jQ_{\rm sref}). \tag{36}$$

The PR current controller using ideal decoupled proportional and reduced-order generalized integrator (ROGI) has following transfer function:

$$\begin{aligned}\boldsymbol{v}^{\rm PR}_{{\rm c},\alpha\beta} &= \boldsymbol{v}^{\rm PR}_{{\rm c1},\alpha\beta} + \tilde{\boldsymbol{v}}^{\rm PR}_{{\rm ch},\alpha\beta} \\ &= -L_{\rm f}\left(K_{\rm p} + \frac{K_{\rm i}}{s-j\omega_{\rm s}}\right)(\boldsymbol{i}_{{\rm sref},\alpha\beta} - \boldsymbol{i}_{{\rm s},\alpha\beta}) \\ &\quad - j\omega_{\rm s}L_{\rm f}i_{{\rm s},\alpha\beta} + \boldsymbol{v}_{{\rm sf},\alpha\beta}.\end{aligned} \tag{37}$$

For the sake of reducing the computational burden, the ROGI is often merged into a second-order generalized integrator (SOGI) as $K_{\rm p} + K_{\rm i}/(s-j\omega_{\rm s}) \to K_{\rm p} + 2K_{\rm i}s/(s^2+\omega_s^2)$[22]. The main control of PR using SOGI is different from $G_{{\rm c},\alpha\beta}(s)$. Therefore, to maintain unity, only PR control with ROGI is considered in this article. The control block diagram of the PR control is presented in Fig. 6. The fundamental components in (37) can be reconfigured and expressed in dq reference frame as follows:

$$\begin{aligned}\boldsymbol{v}_{\rm c1,dq} &= -L_{\rm f}\left(K_{\rm p} + \frac{K_{\rm i}}{s'}\right)(\boldsymbol{i}_{\rm sref,dq} - \boldsymbol{i}_{\rm s1,dq}) \\ &\quad - j\omega_{\rm s}L_{\rm f}i_{\rm s1,dq} + \boldsymbol{v}_{\rm s1,dq}.\end{aligned} \tag{38}$$

By substituting (38) into (3), the transient dynamics of the fundamental current component tracking can be derived as the same as (9). Therefore, it can be concluded that the S-VOC and PR share the same power tracking property. By dividing the current input into $\boldsymbol{i}_{{\rm s},\alpha\beta} = \boldsymbol{i}_{{\rm s1},\alpha\beta} + \tilde{\boldsymbol{i}}_{{\rm sh},\alpha\beta}$, the harmonic components of the VSC output voltage can be deduced by substituting (36) into (37) as

$$\tilde{\boldsymbol{v}}_{{\rm ch},\alpha\beta} = G_{\rm del}(s)G_{{\rm c},\alpha\beta}(s)\tilde{\boldsymbol{i}}_{{\rm sh},\alpha\beta} + G_{\rm del}(s)G_{\rm fil}(s)[1+G_{\rm PR}(s)]\tilde{\boldsymbol{v}}_{{\rm sh},\alpha\beta} \tag{39}$$

where $G_{\rm PR}(s)$ can be expressed as

$$G_{\rm PR}(s) = \frac{2L_{\rm f}}{3|\boldsymbol{v}^2_{\rm s1}|}\left(K_{\rm p} + \frac{2K_{\rm i}s}{s^2+\omega_s^2}\right)(P_{\rm sref} - jQ_{\rm sref}). \tag{40}$$

The coupling in $|\boldsymbol{v}^2_{\rm sf}|$ is not considered in the admittance model, i.e., $|\boldsymbol{v}^2_{\rm sf}|$ is simplified as a known constant $|\boldsymbol{v}^2_{\rm s1}|$ in (40). Note that a constant value $|\boldsymbol{v}^2_{\rm s1}|$ can be used to replace the real-time calculation of $|\boldsymbol{v}^2_{\rm sf}|$ in (36) for the sake of eliminating the coupling terms. However, it sacrifices the accuracy of power tracking once the system operation point changes.

The harmonic admittance of the VSC using PR control can be derived by substituting (39) into (4) as follows:

$$\boldsymbol{Y}^{\rm PR}_{\rm VSC} = \frac{\tilde{\boldsymbol{i}}_{{\rm sh},\alpha\beta}}{\tilde{\boldsymbol{v}}_{{\rm sh},\alpha\beta}} = Y^{\rm PI}_{\rm VSC} + Y^{\rm PR}_{\rm n} \tag{41}$$

where $Y^{\rm PR}_{\rm n}$ denotes the influence of PR control on VSC system admittance

$$\begin{aligned}\boldsymbol{Y}^{\rm PR}_{\rm n} &= -[1+G_{\rm del}(s)Y_{\rm f}(s)G_{{\rm c},\alpha\beta}(s-j\omega_{\rm s})]^{-1} \\ &\quad \cdot Y_{\rm f}(s)G_{\rm del}(s)G_{\rm fil}(s)G_{\rm PR}(s).\end{aligned} \tag{42}$$

C. VM-DPC Control

VM-DPC is a symmetrical control strategy designed directly in $\alpha\beta$ reference frame. The method guarantees power tracking without using PLL with zero steady-state error. A brief introduction of the control scheme is presented first in this subsection. The instantaneous powers of the VSC can be expressed as

$$\begin{cases} P_{\rm sf} = P_{\rm s1} + P_{\rm shf} = -\frac{3}{2}{\rm Re}(\boldsymbol{v}_{\rm sf}\boldsymbol{i}^*_{\rm s}) \\ Q_{\rm sf} = Q_{\rm s1} + Q_{\rm shf} = -\frac{3}{2}{\rm Im}(\boldsymbol{v}_{\rm sf}\boldsymbol{i}^*_{\rm s}) \end{cases} \tag{43}$$

where $P_{\rm shf}$ and $Q_{\rm shf}$ denote the instantaneous powers generated by the harmonics of PCC voltage and output current. $\boldsymbol{i}^*_{\rm s}$ is the

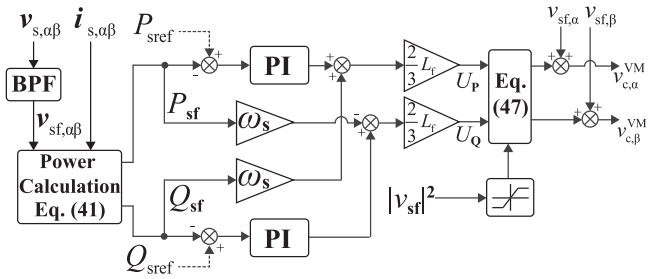

Fig. 7. Control scheme of voltage modulated direct power control (VM-DPC).

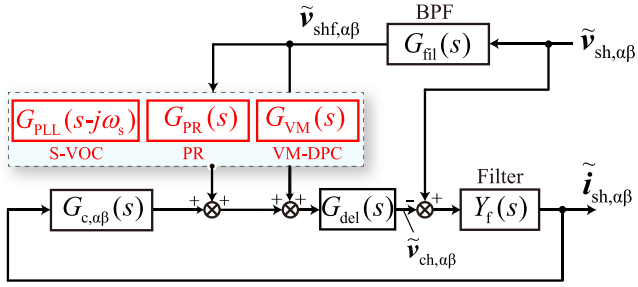

Fig. 8. Small-signal block diagram of grid-connected VSC using three symmetrical control strategies with BPF and voltage feedforward.

conjugate of $\boldsymbol{i}_{\rm s}$. The differential of powers is presented as

$$\begin{cases} \frac{dP_{\rm sf}}{dt} = -\frac{3}{2}{\rm Re}\left(\frac{d\boldsymbol{v}_{{\rm sf},\alpha\beta}}{dt}\boldsymbol{i}^*_{{\rm s},\alpha\beta}\right) - \frac{3}{2}{\rm Re}\left(\boldsymbol{v}_{{\rm sf},\alpha\beta}\frac{d\boldsymbol{i}^*_{{\rm s},\alpha\beta}}{dt}\right) \\ \frac{dQ_{\rm sf}}{dt} = -\frac{3}{2}{\rm Im}\left(\frac{d\boldsymbol{v}_{{\rm sf},\alpha\beta}}{dt}\boldsymbol{i}^*_{{\rm s},\alpha\beta}\right) - \frac{3}{2}{\rm Im}\left(\boldsymbol{v}_{{\rm sf},\alpha\beta}\frac{d\boldsymbol{i}^*_{{\rm s},\alpha\beta}}{dt}\right). \end{cases} \tag{44}$$

Note that the VM-DPC is designed based on an ideal grid voltage condition. Therefore, the differential of filtered grid voltage can be approximated as

$$\frac{d}{dt}\boldsymbol{v}_{{\rm sf},\alpha\beta} \approx j\omega_{\rm s}\boldsymbol{v}_{{\rm sf},\alpha\beta}. \tag{45}$$

By substituting (2) and (45) into (44), the instantaneous variation of the active and reactive powers of VSC can be calculated as

$$\begin{cases} \frac{dP_{\rm sf}}{dt} = -\omega_{\rm s}Q_{\rm sf} - \frac{R_{\rm f}}{L_{\rm f}}P_{\rm sf} + \frac{3}{2L_{\rm f}}U_{\rm P} \\ \frac{dQ_{\rm sf}}{dt} = \omega_{\rm s}P_{\rm sf} - \frac{R_{\rm f}}{L_{\rm f}}Q_{\rm sf} + \frac{3}{2L_{\rm f}}U_{\rm Q} \end{cases} \tag{46}$$

where $U_{\rm P}$ and $U_{\rm Q}$ are the power regulation inputs, which are

$$\begin{aligned} U_{\rm P} &= {\rm Re}(\boldsymbol{v}_{{\rm sf},\alpha\beta}\boldsymbol{v}^*_{{\rm c},\alpha\beta}) - |\boldsymbol{v}^2_{\rm sf}| \\ U_{\rm Q} &= {\rm Im}(\boldsymbol{v}_{{\rm sf},\alpha\beta}\boldsymbol{v}^*_{{\rm c},\alpha\beta}). \end{aligned} \tag{47}$$

Based on (46) and (47), the power tracking can be designed in closed-loop using PI and power feedforward, which can be expressed as follows:

$$\begin{cases} U_{\rm P} = \frac{2L_{\rm f}}{3}G_{{\rm PI,dq}}(s')(P_{\rm sref} - P_{\rm sf}) + \omega_{\rm s}Q_{\rm sf} \\ U_{\rm Q} = \frac{2L_{\rm f}}{3}G_{{\rm PI,dq}}(s')(Q_{\rm sref} - Q_{\rm sf}) - \omega_{\rm s}P_{\rm sf}. \end{cases} \tag{48}$$

Finally, the output VSC voltage can be decomposed into its fundamental and harmonic components as $\boldsymbol{v}^{\rm VM}_{{\rm c},\alpha\beta} = \boldsymbol{v}^{\rm VM}_{{\rm c1},\alpha\beta} + \boldsymbol{v}^{\rm VM}_{{\rm ch},\alpha\beta}$, which can be deduced from (47) and given as

$$\begin{cases} v^{\rm VM}_{{\rm c},\alpha} = (v_{{\rm sf},\alpha}U_{\rm P} + v_{{\rm sf},\beta}U_{\rm Q})/|\boldsymbol{v}^2_{\rm sf}| + v_{{\rm sf},\alpha} \\ v^{\rm VM}_{{\rm c},\beta} = (v_{{\rm sf},\beta}U_{\rm P} - v_{{\rm sf},\alpha}U_{\rm Q})/|\boldsymbol{v}^2_{\rm sf}| + v_{{\rm sf},\beta}. \end{cases} \tag{49}$$

Note that by substituting (43) and (48) into (46), the dynamics of the fundamental power tracking can be extracted and expressed in terms of the same equation given as (9)

$$\frac{\boldsymbol{S}_{\rm s1}}{\boldsymbol{S}_{\rm sref}} = \frac{K_{\rm p}s' + K_{\rm i}}{s'^2 + (K_{\rm p} + \frac{R_{\rm f}}{L_{\rm f}})s' + K_{\rm i}}. \tag{50}$$

Therefore, it is found that VM-DPC and VOC share the same power tracking property. Moreover, VM-DPC has better tracking performance since it eliminates PLL [26]. The control scheme of VM-DPC is presented in Fig. 7.

It can be found from (49) that the integration control of the powers inevitably results in a cross-coupling between harmonic components and fundamental components. However, if the magnitude $\tilde{\boldsymbol{v}}_{\rm shf}$ can be reduced by using the BPF, then $\tilde{\boldsymbol{v}}^{\rm VM}_{{\rm ch},\alpha\beta}$ can be approximately linearized [30]. The details of the linearization of $\tilde{\boldsymbol{v}}^{\rm VM}_{{\rm ch},\alpha\beta}$ are presented as

$$\begin{aligned} \tilde{\boldsymbol{v}}^{\rm VM}_{{\rm ch},\alpha\beta} &= G_{\rm del}(s)G_{{\rm c},\alpha\beta}(s)\tilde{\boldsymbol{i}}_{{\rm sh},\alpha\beta} \\ &\quad + G_{\rm del}(s)G_{\rm fil}(s)[1 + G_{\rm VM}(s)]\tilde{\boldsymbol{v}}_{{\rm sh},\alpha\beta} \end{aligned} \tag{51}$$

where $G_{{\rm c},\alpha\beta}(s)$ can be found equal to $G_{{\rm c,dq}}(s')$ as follows:

$$G_{{\rm c},\alpha\beta}(s) = L_{\rm f}\left(K_{\rm p} + \frac{K_{\rm i}}{s - j\omega_{\rm s}} - j\omega_{\rm s}\right) = G_{{\rm c,dq}}(s') \tag{52}$$

and $G_{\rm VM}(s)$ can be written as

$$G_{\rm VM}(s) = \frac{2L_{\rm f}K_{\rm p}}{3|\boldsymbol{v}^2_{\rm s1}|}(P_{\rm sref} - jQ_{\rm sref}). \tag{53}$$

The detailed admittance model of VSC using VM-DPC can be derived by substituting (51) into (4). The admittance model can be derived as

$$\boldsymbol{Y}^{\rm VM}_{\rm VSC} = \frac{\tilde{\boldsymbol{i}}_{{\rm sh},\alpha\beta}}{\tilde{\boldsymbol{v}}_{{\rm sh},\alpha\beta}} = Y^{\rm PI}_{\rm VSC} + Y^{\rm VM}_{\rm n} \tag{54}$$

where $Y^{\rm VM}_{\rm n}$ denotes the virtual admittance of VM-DPC, which represents the adverse effect of the VM-DPC on the basic admittance $Y^{\rm PI}_{\rm VSC}$. The expression of $Y^{\rm VM}_{\rm n}$ is

$$\begin{aligned} \boldsymbol{Y}^{\rm VM}_{\rm n} = &-[1 + G_{\rm del}(s)Y_{\rm f}(s)G_{{\rm c},\alpha\beta}(s - j\omega_{\rm s})]^{-1} \\ &\cdot Y_{\rm f}(s)G_{\rm del}(s)G_{\rm fil}(s)G_{\rm VM}(s). \end{aligned} \tag{55}$$

Finally, the small-signal block diagram of three symmetrical control strategies can be unified using the same frame as shown in Fig. 8. The differences of the block diagram of three methods are highlighted in red color. By comparing (53) with (40), it can be found that the difference between $G_{\rm PR}(s)$ and $G_{\rm VM}(s)$ can be deduced as

$$G_{\rm PR}(s) - G_{\rm VM}(s) = \frac{2L_{\rm f}}{3|\boldsymbol{v}^2_{\rm s1}|}\frac{2K_{\rm i}}{s^2 + \omega_s^2}(P_{\rm sref} - jQ_{\rm sref}). \tag{56}$$

It shows that the difference between $Y^{\rm PR}_{\rm VSC}$ and $Y^{\rm VM}_{\rm VSC}$ gets larger when the frequency of the harmonics is close to the fundamental frequency, i.e., $s = j\omega_{\rm h} \approx j\omega_{\rm s}$. On the other side, when $\omega_{\rm h}$ is away from $\omega_{\rm s}$, it can be assumed that $Y^{\rm PR}_{\rm VSC} \approx Y^{\rm VM}_{\rm VSC}$ in the high- and low-frequency range.

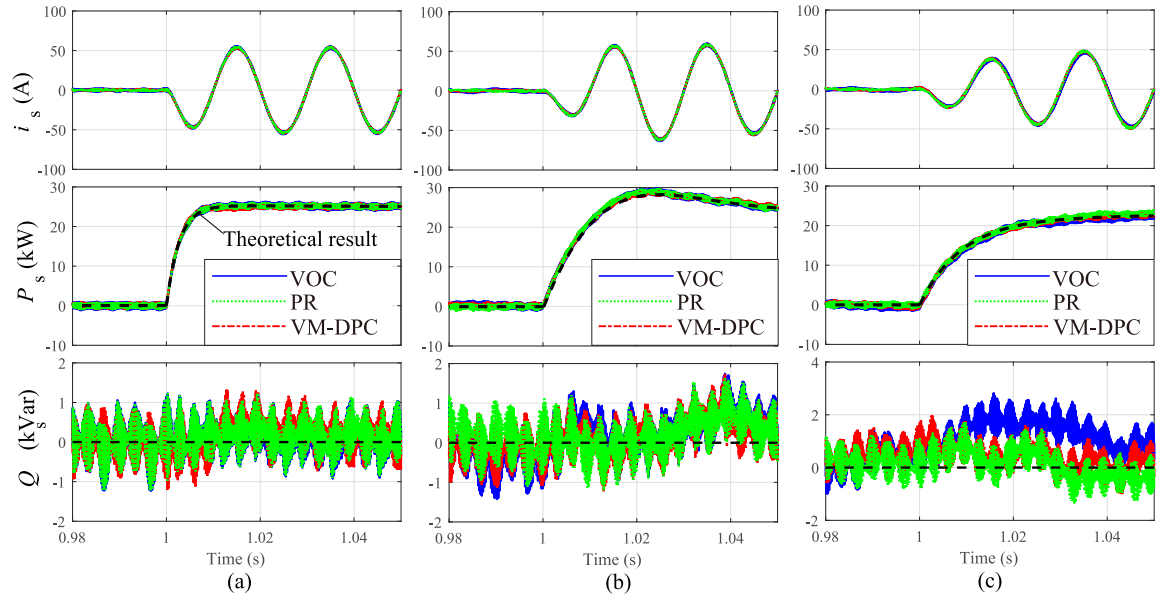

Fig. 9. Transient dynamics comparison of three different control methods under different control parameters. (a) $\omega_n = 100$ and $\zeta = 2$. (b) $\omega_n = 100$ and $\zeta = 0.7$. (c) $\omega_n = 30$ and $\zeta = 2$.

TABLE I
PARAMETERS OF SIMULATED GRID-CONNECTED VSC SYSTEM AND VM-DPC CONTROLLER

Parameter	Symbol	Value	Unit
Rated power	$P_{\rm sref}$	25	kW
Switching frequency	$f_{\rm w}$	4	kHz
Sampling frequency	$f_{\rm sa}$	4	kHz
Time delay	$T_{\rm del}$	0.0001	s
Fundamental frequency	f	50	Hz
Ground-to-line Voltage	$v_{\rm s,rms}$	220	V
Natural frequency of BPF	$\omega_{\rm fn}$	314	rad/s
Damping ratio of BPF	$\zeta_{\rm f}$	0.1	
Dc voltage	$v_{\rm dc}$	730	V
Filter resistance	$R_{\rm f}$	0.12	Ω
Filter inductor	$L_{\rm f}$	6	mH
Control Parameters			
Parameter	Value	Parameter	Value
$K_{\rm p}$	121.4	$K_{\rm i}$	10000
$\omega_{\rm n}$	100	ζ	0.7
$K_{\rm PLL,p}$	1.5	$K_{\rm PLL,i}$	130
$f_{\rm bw\_PLL}$	100 Hz		

IV. UNIFIED PERFORMANCE ANALYSIS

The unified dynamic response of three control strategies is discussed in this section. The power tracking dynamics of three controllers can be deduced by transforming (9) and (50) into the time domain as follows:

$$\begin{cases} \boldsymbol{S}_{\rm s} = \boldsymbol{S}_{\rm sref}\{1+e^{-\zeta\omega_n t}[(\frac{K_{\rm p}}{\omega_d}-\frac{\zeta}{\sqrt{1-\zeta^2}})\sin(\omega_d t) \\ \quad -\cos(\omega_d t)]\},\ \zeta<1 \\ \boldsymbol{S}_{\rm s} = \boldsymbol{S}_{\rm sref}\{1+e^{-\zeta\omega_n t}[(\frac{K_{\rm p}}{\omega_d}-\frac{\zeta}{\sqrt{\zeta^2-1}})\sinh(\omega_d t) \\ \quad -\cosh(\omega_d t)]\},\ \zeta>1 \end{cases} \tag{57}$$

where $\omega_{\rm d} = \omega_{\rm n}\sqrt{1-\zeta^2}$ denotes the natural damping frequency. To compare the transient response characteristics of different control strategies, a simulation is carried out in MATLAB/Simulink Simscape Power System. The IGBT switching signals are generated by using space vector pulsewidth modulation (SVPWM) with a switching frequency of 4 kHz.The dc-link voltage is set to 730 V. The VSC is connected to an ideal power grid. The circuit and control parameters are presented in Table I. Fig. 9 shows the simulation result of system step response with different control parameters. $\Delta P_{\rm sref} = 25$ kW is set at 1 s. Three different control settings are chosen, i.e., ($\omega_{\rm n} = 100$ and $\zeta = 2$), ($\omega_{\rm n} = 100$ and $\zeta = 0.7$), and ($\omega_{\rm n} = 30$ and $\zeta = 2$). The black dotted line shows the dynamics response calculated based on (57). They are in agreement with the simulation results. It can be recognized that all three VSCs with different control methods track their references very well. Moreover, they also exhibit a similar transient response. The couplings between active and reactive power regulation of three methods are all small. It can be concluded that three different control methods have the same power tracking property. It can also be found that the system transient performance is improved either by increasing $\omega_{\rm n}$ from 30 to 100 or increasing ζ from 0.7 to 2.

Note that the transient responses in Fig. 9 are obtained under ideal grid conditions. The steady-state performance of VSC using different controllers is also tested under nonideal grid conditions as presented in Fig. 10. The system performance under frequency variation conditions is shown in Fig. 10(a). It can be observed that the PR control strategy leads to a steady-state error in the reactive power output. The system performance under three-phase voltage drop (0.2 p.u.) and phase-A voltage drop (0.2 p.u.) are tested, respectively, as presented in Fig. 10(b) and (c). It can be observed that three control strategies exhibit similar steady-state performance under the voltage drop conditions. In addition, note that the unbalanced voltage drop will cause power fluctuation and harmonic components. The reactive power fluctuation of VSC using the S-VOC is relatively large among

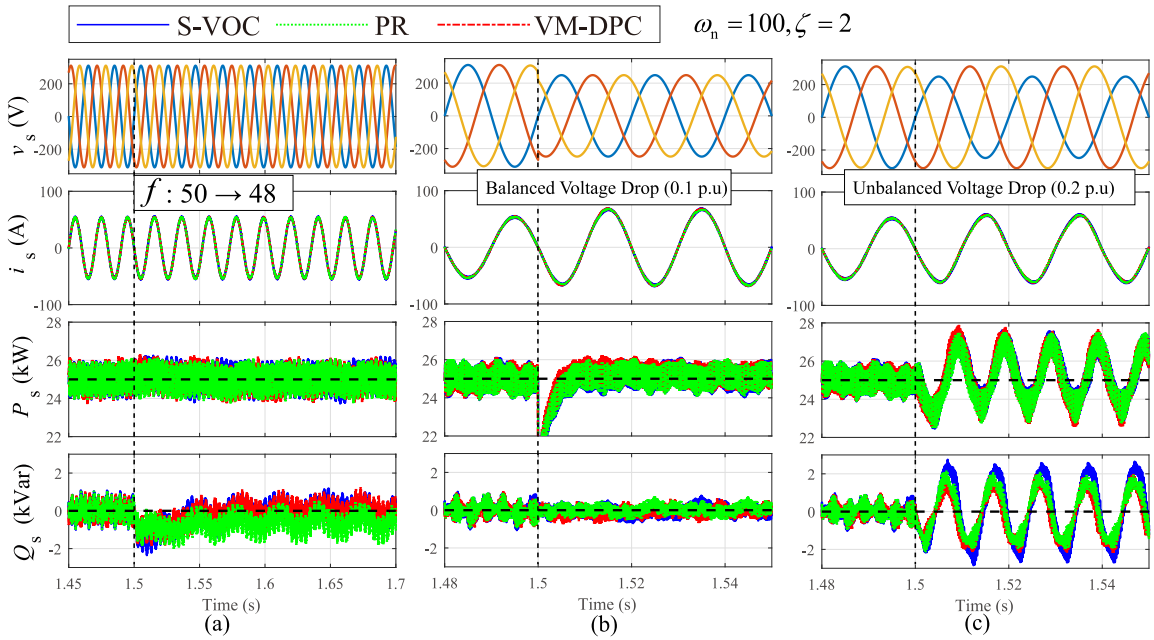

Fig. 10. Transient dynamics comparison of three different control methods under nonideal grid conditions. (a) Frequency variation. (b) Balanced voltage drop condition. (c) Unbalanced voltage drop condition.

the three control strategies, which is caused by the error of phase-locking under unbalanced grid conditions.

In this section, the unified transient performance of three control methods is analyzed. Note that once the control parameters are determined, the basic admittance $Y_{\mathrm{VSC}}^{\mathrm{PI}}$ is also determined. However, since each strategy has different additional admittance, their influence will affect the admittance characteristics and the grid-connection stability. In Section V, the admittance of three control methods is analyzed, and the accuracy of the admittance modeling is verified using the frequency-scan method. Moreover, the stability of the three control methods is compared based on the unified power tracking dynamics. In order to better explain the work of this article, a diagram that summarizes the structure is presented in Fig. 11.

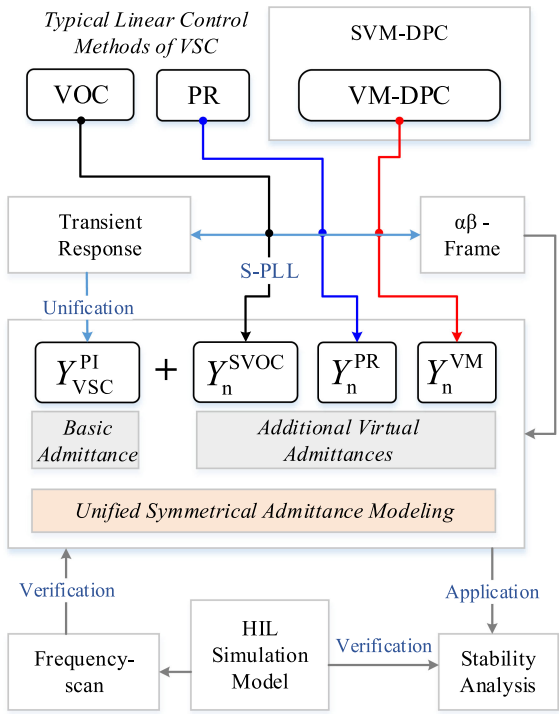

Fig. 11. Structure of the article.

V. Admittance Specification and Stability Analysis

This section determines the admittance specifications of the three control strategies. The circuit and control parameters are the same as those presented in Table I.

A. Admittance Model Verification

The accuracy of the proposed admittance modeling can be verified through the frequency-scan method. The bode plots of the proposed admittance characteristic calculated based on (34), (54), and (41) are compared with the corresponding frequency-scan results as presented in Fig. 12. The frequency-scan results are carried out using detailed models which consider both the time delay and PWM. The control parameters of the comparison study is chosen as ($K_{\mathrm{p}} = 121, K_{\mathrm{i}} = 10000 \rightarrow \omega_{\mathrm{n}} = 100$ and $\zeta = 0.7$). The bandwidth of the symmetrical PLL is set to $f_{\mathrm{bw\_PLL}} = 100$ Hz. It can be observed that the harmonic responses of grid-connected VSC using S-VOC and PR are very close to each other. The difference of admittance characteristics is mainly reflected near the fundamental frequency (50 Hz), that the VSC using VM-DPC exhibits a comparatively low admittance magnitude, followed by the PR control and the S-VOC.

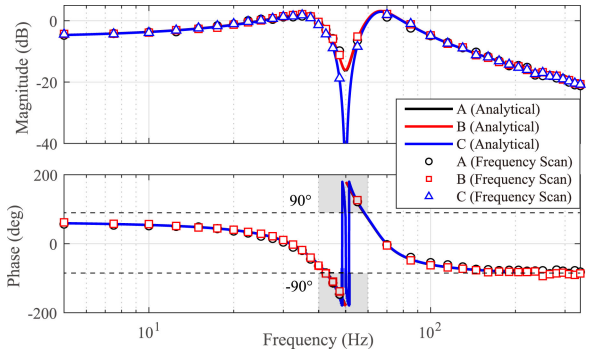

Fig. 12. Verification of the proposed admittance modeling with different control strategies ($\omega_n = 100$ and $\zeta = 0.7$). (A) S-VOC. (B) PR control. (C) VM-DPC.

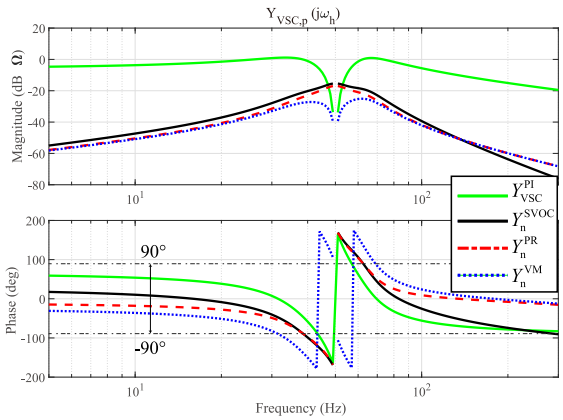

Fig. 13. Comparison between the basic admittance $Y_{\mathrm{VSC}}^{\mathrm{PI}}$ and the virtual admittances of different symmetrical control methods.

Among the three control strategies, the S-VOC appears most sensitive to voltage harmonics, while VM-DPC seems to be the most robust one.

The adverse effect of the control structures on the equivalent admittance characteristics of grid-connected VSC is studied by comparing $Y_{\mathrm{VSC}}^{\mathrm{PI}}$ to the virtual admittances $Y_{\mathrm{n}}^{\mathrm{SVOC}}$, $Y_{\mathrm{n}}^{\mathrm{VM}}$, and $Y_{\mathrm{n}}^{\mathrm{PR}}$, as presented in Fig. 13. It can be observed that in the high- and low-frequency range, the admittance characteristic of grid-connected VSC is mostly determined by the basic admittance $Y_{\mathrm{VSC}}^{\mathrm{PI}}$ since $Y_{\mathrm{VSC}}^{\mathrm{PI}} \gg (Y_{\mathrm{n}}^{\mathrm{SVOC}}, Y_{\mathrm{n}}^{\mathrm{VM}}, Y_{\mathrm{n}}^{\mathrm{PR}})$. The virtual admittances $Y_{\mathrm{n}}^{\mathrm{VM}}$, $Y_{\mathrm{n}}^{\mathrm{SVOC}}$, and $Y_{\mathrm{n}}^{\mathrm{PR}}$ successively show the negative damping characteristics, i.e., their phases are not within –90° to 90°, when the frequency moves close to 50 Hz. Since $Y_{\mathrm{n}}^{\mathrm{VM}}$ exhibits the lowest magnitude, the negative damping of VM-DPC is the smallest among three strategies, which shows consistency with Fig. 12.

Fig. 14 shows a comparison of the analytical and frequency-scan results of the VSC equivalent admittances using different control strategies. The three different controllers are compared in separated figures. In each figure, the lines and dots with the same color denote the controllers that have the same control parameters. In other words, they share the same basic admittance $Y_{\mathrm{VSC}}^{\mathrm{PI}}$. Three groups of control parameters are selected: group (A) denotes ($K_{\mathrm{p}} = 380, K_{\mathrm{i}} = 10000 \rightarrow \omega_{\mathrm{n}} = 100$ and $\zeta = 2$); group (B) denotes ($K_{\mathrm{p}} = 121, K_{\mathrm{i}} = 10000 \rightarrow \omega_{\mathrm{n}} = 100$ and $\zeta = 0.7$); and group (C) denotes ($K_{\mathrm{p}} = 100, K_{\mathrm{i}} = 900 \rightarrow \omega_{\mathrm{n}} = 30$ and $\zeta = 2$), respectively. Moreover, when the parameters of the main controller change, the Bode plots of $Y_{\mathrm{VSC}}^{\mathrm{SVOC}}$, $Y_{\mathrm{VSC}}^{\mathrm{VM}}$, and $Y_{\mathrm{VSC}}^{\mathrm{PR}}$ show similar variation rules. The results indicate that the decrease of damping ratio ζ and natural frequency ω_{n} will increase the magnitude of the system admittances, i.e., the system tends to be more sensitive to the

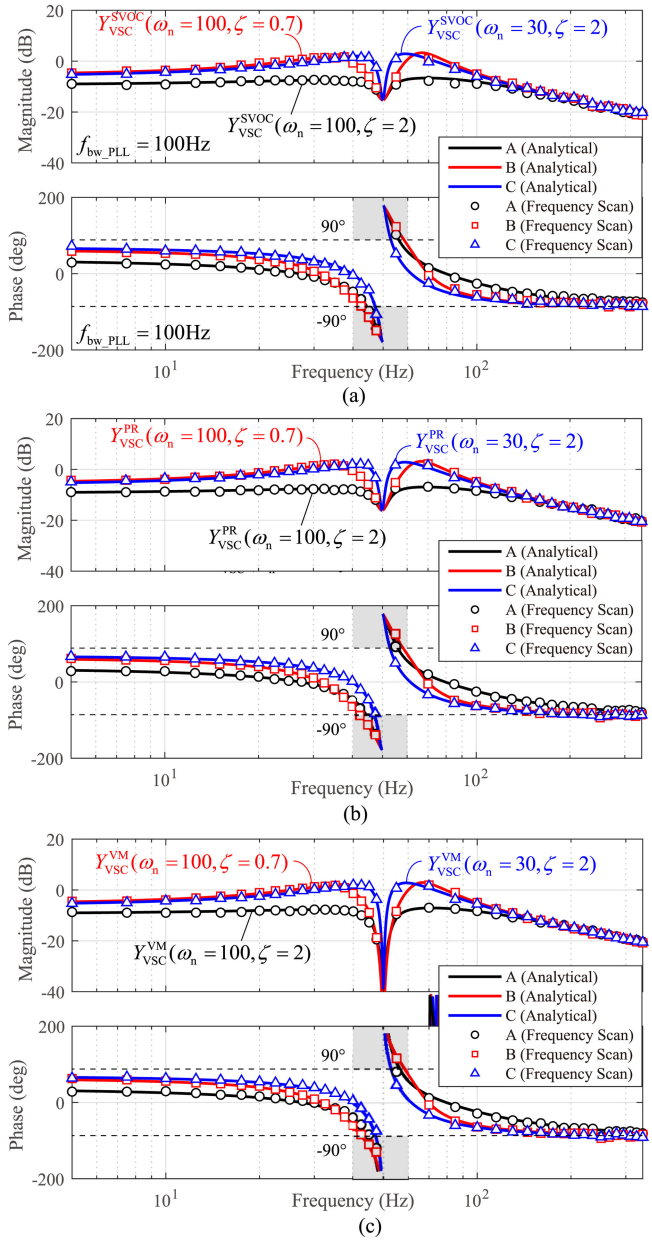

Fig. 14. Verification of the proposed admittance modeling under different control settings by using frequency-scan method. (a) $Y_{\mathrm{VSC}}^{\mathrm{SVOC}}$. (b) $Y_{\mathrm{VSC}}^{\mathrm{PR}}$. (c) $Y_{\mathrm{VSC}}^{\mathrm{VM}}$. (A) $\omega_{\mathrm{n}} = 100$ rad/s and $\zeta = 0.7$. (B) $\omega_{\mathrm{n}} = 100$ rad/s and $\zeta = 2$. (C) $\omega_{\mathrm{n}} = 20$ rad/s and $\zeta = 0.7$.

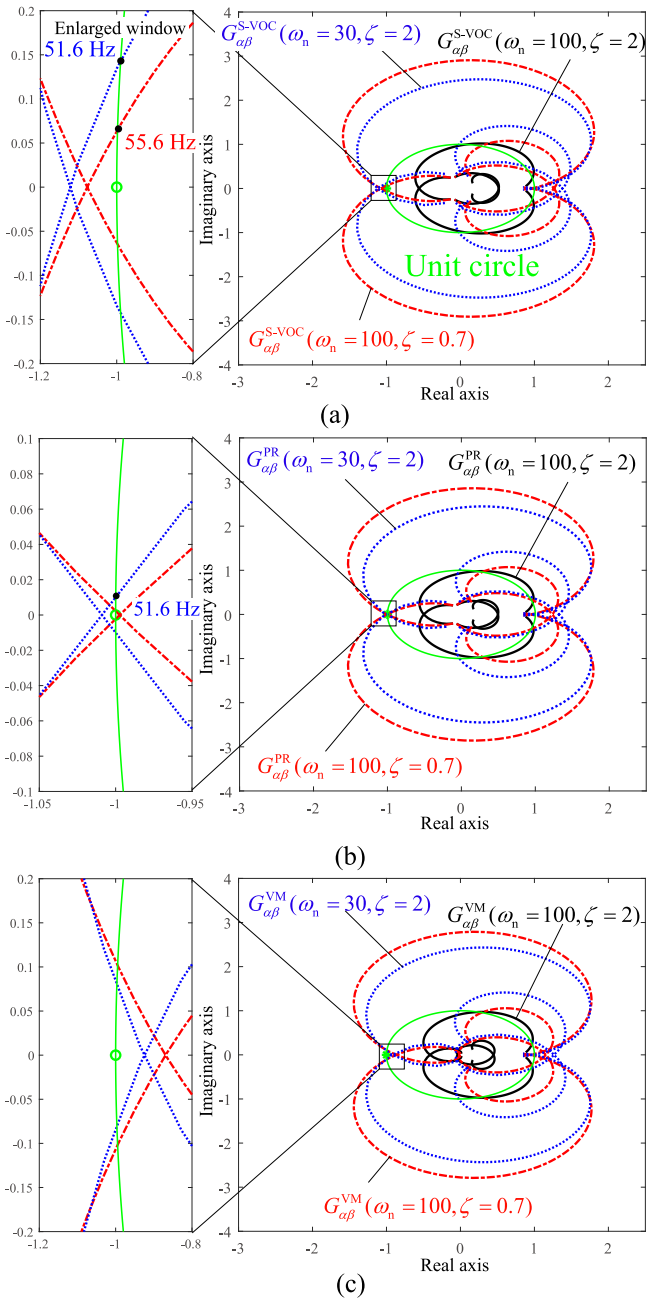

Fig. 15. Comparison of the Nyquist plots of three control methods with different control parameters.

voltage harmonics and becomes less stable under weak-grid connected conditions.

B. Stability Analysis

In this subsection, the availability of the proposed method is verified by using the Nyquist stability criterion and simulation results. The grid admittance can be assumed as a simple, balanced *R-L* circuit, which can be expressed under the $\alpha\beta$ reference frame by using Laplace-transform as follows:

$$Y_{\text{grid}}(s)=\frac{1}{L_{\text{n}}s+R_{\text{n}}} \tag{58}$$

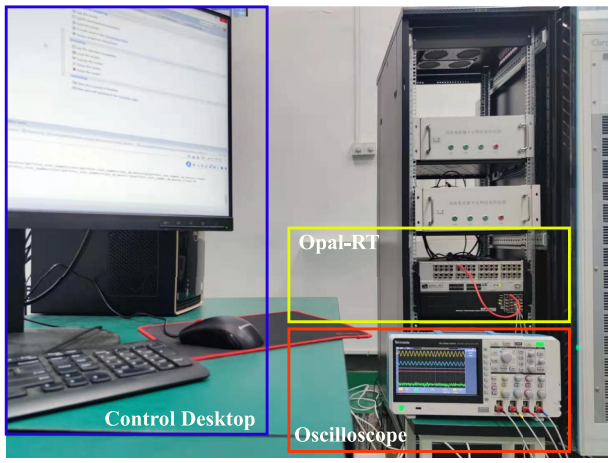

Fig. 16. Real-time simulation platform RTLAB from OPAL-RT for testing the three control methods.

where R_{n} is the grid resistance and L_{n} is the grid series inductance. The stability of the grid-connected VSC can be identified by using simple SISO Nyquist stability criterion [4]. The system can be simplified as Thevenin equivalent circuit consisting of the equivalent VSC admittance represented by Y_{VSC}, which are derived in (34), (54), and (41), respectively, and the grid admittance Y_{grid}. The stability of the system can be identified by the eigenvalues of the transfer function given as

$$H_{\text{s}}=\frac{1}{1+G_{\alpha\beta}(s)} \tag{59}$$

where $G_{\alpha\beta}(s)=Y_{\text{VSC}}(s)/Y_{\text{grid}}(s)$ is the feedback characteristic equation of the system. Based on the linear-control theory that the closed-loop transfer function H_{s} guarantees stable operation only if $G_{\alpha\beta}(s)$ satisfies the Nyquist stability criterion, i.e., the encirclement of $(-1,j0)$ by the admittance ratio $G_{\alpha\beta}(s)$ is zero.

Fig. 15 shows a comparison of the Nyquist plot of $G_{\alpha\beta}(s)$ using different control methods. The VSCs are considered to be connected with grid with equivalent impedance ($L_{\text{n}}=4.5$ mH and $R_{\text{n}}=0.6\ \Omega$). Three different control parameter settings are chosen as the same as in Fig. 14. The bandwidth of the symmetrical PLL is set to 100 Hz. Fig. 15(a) shows the Nyquist diagram of $G_{\alpha\beta}(s)$ describing a grid-connected VSC using S-VOC. It can be seen that the encirclement around $(-1,0)$ of the Nyquist curve $Y_{\text{VSC}}^{\text{SVOC}}(s)/Y_{\text{grid}}(s)$ is zero when $\omega_{\text{n}}=100$ and $\zeta=2$. However, the system becomes unstable when ζ changes from 2 to 0.7 and ω_{n} keeps 100 since the Nyquist curve encircles $(-1+j0)$. It can be also found that the Nyquist curve intersects unit circle at 55.6 Hz, which also indicates the frequency of the oscillation component. It can also be found that when ω_{n} changes from 100 to 30 while $\zeta=0.7$, the Nyquist curve encircles $(-1+j0)$ and intersects unit circle at 51.9 Hz. From the enlarged window of Fig. 15(b), it can be found that the point of intersection indicating $\omega_{\text{n}}=100$ and $\zeta=0.7$, and $\omega_{\text{n}}=30$ and $\zeta=2$, are very close to the critical point. Therefore, the system will be unstable. $G_{\alpha\beta}^{\text{PR}}$ with $\omega_{\text{n}}=30$ and $\zeta=2$ intersects the unit circle at 51.9 Hz. From Fig. 15(c), it can be found that all three curves avoid the critical point.

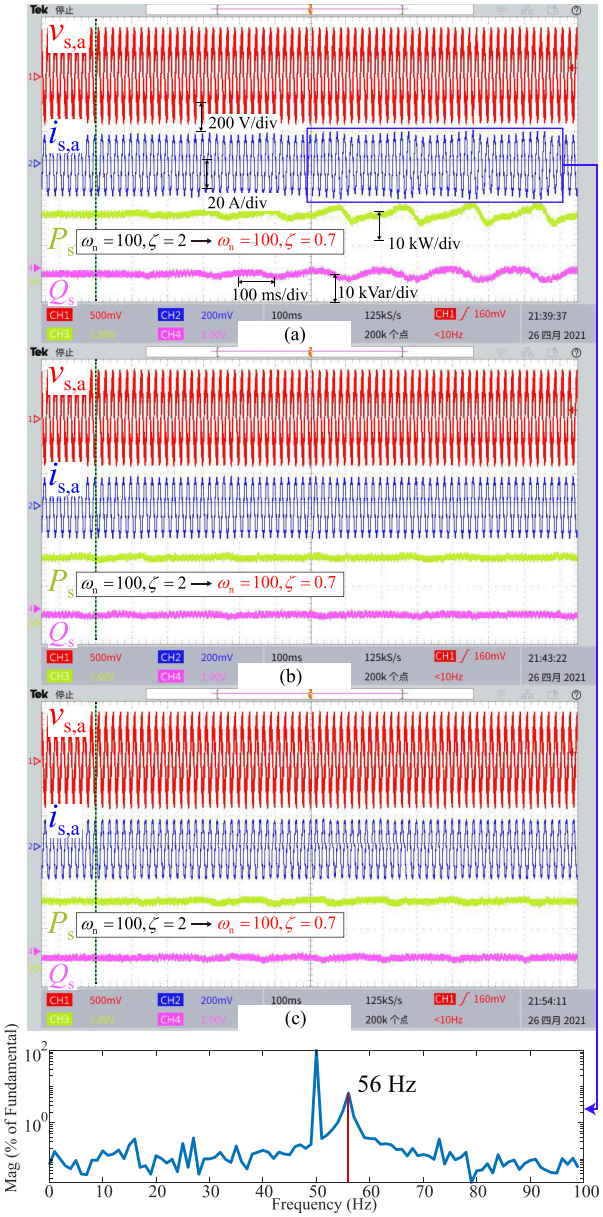

Fig. 17. Comparison of the grid interconnection test of the systems using different control methods when ($\omega_n = 100$ and $\zeta = 0.7$). (a) VOC with symmetrical PLL ($f_{bw\_PLL} = 100$). (b) PR. (c) VM-DPC.

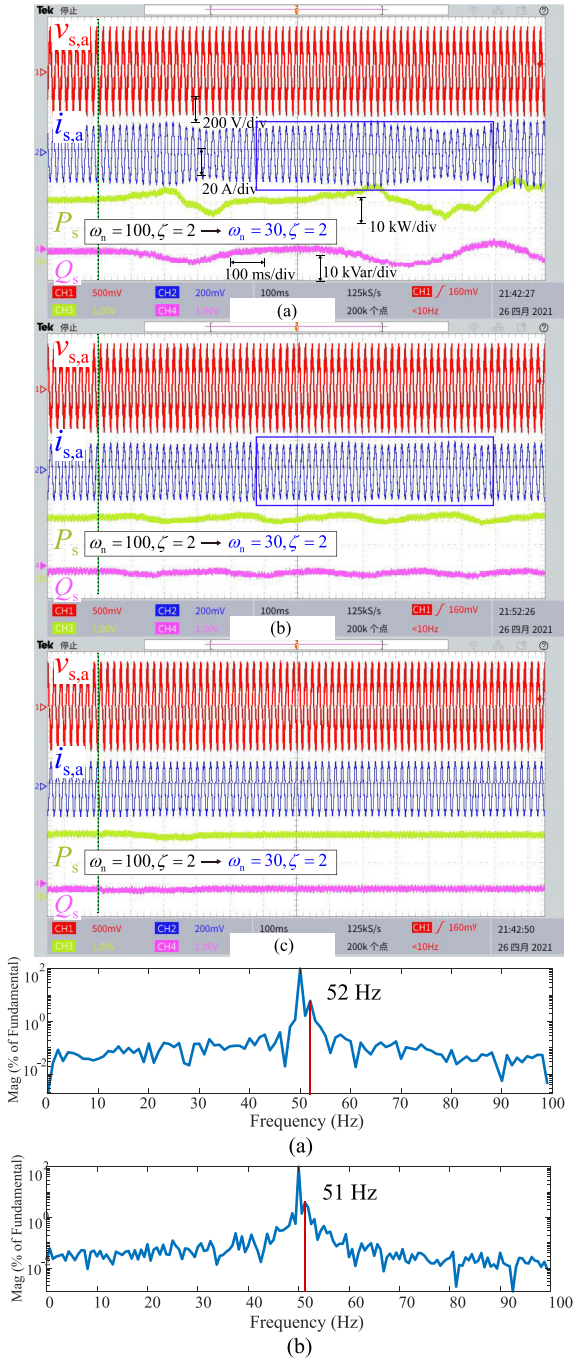

Fig. 18. Comparison of the grid interconnection test of the systems using different control methods under ($\omega_n = 30$ and $\zeta = 2$). (a) VOC with symmetrical PLL ($f_{bw\_PLL} = 100$). (b) PR. (c) VM-DPC.

Therefore, it can be concluded that the grid-connected VSC using the VM-DPC can maintain stable with all three control parameter settings.

The effectiveness of the Nyquist stability criterion based on the proposed admittance modeling method is verified using detailed simulation models implemented in real-time simulation platform RTLAB from Opal-RT as shown in Fig. 16. The circuit and the control parameters of the test are set as presented in Table I. Both time delay and PWM are considered in the simulation model. The VSCs are initially connected to a grid with equivalent impedance set as an inductor $L_n = 4.5$ mH in series with a resistance $R_n = 0.6\ \Omega$. In Fig. 17, the control parameters are set to ($\omega_n = 100$ and $\zeta = 2$) at the beginning of the simulation. Then, the control parameters of three systems change to ($\omega_n = 100$ and $\zeta = 0.7$). The results indicate that the grid-connected VSC using S-VOC becomes unstable. The frequency of the main oscillation component is 56 Hz, which is consistent with the Nyquist stability analysis. On the other side, the VSC using the VM-DPC and PR still maintain stability after the change. Fig. 18 demonstrates the cases of changing the control parameters from ($\omega_n = 100$ and $\zeta = 2$) to ($\omega_n = 30$ and $\zeta = 2$). It can be observed that VSCs using S-VOC and

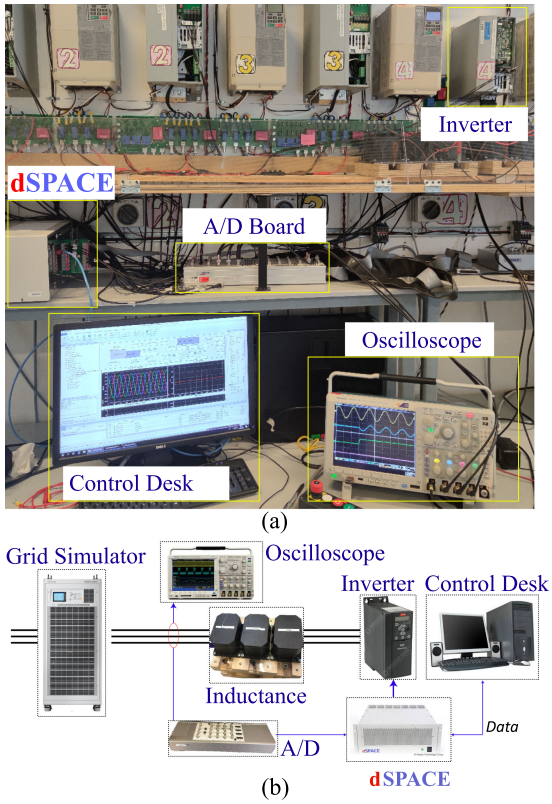

Fig. 19. Experimental setup at Aalborg University.

TABLE II
PROS AND CONS OF THE THREE CONTROL STRATEGIES

Control	Advantages	Disadvantages
VOC (PLL) (S-PLL)	· Robust to parameter/ frequency variations · Measurement of grid frequency · No frequency coupling	· Use of coordinate transformation (dq frame) · Complex control structure · Frequency-coupling · Use of voltage magnitude
PR	· Simple structure	· Affected by frequency variation
VM-DPC	· Robust to parameter/ frequency variations · Strong grid-connection stability · No coordinate transformation · Simple structure	· PI control brings frequency-coupling

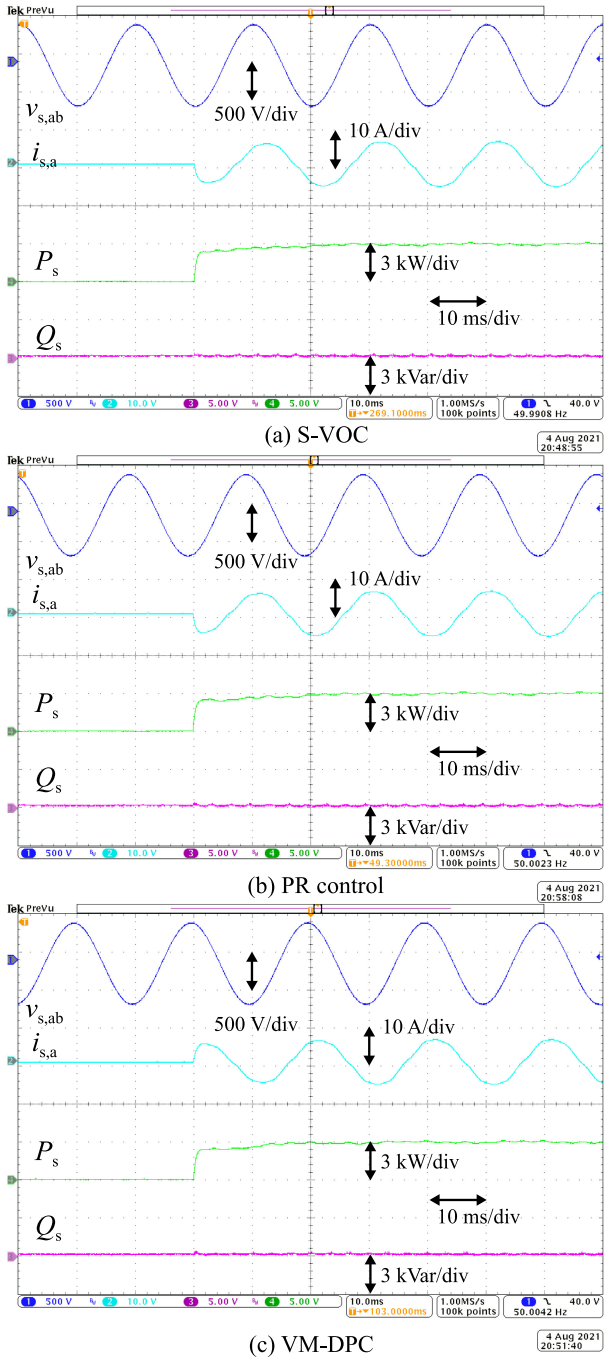

Fig. 20. Transient dynamics comparison of three different control methods. (a) S-VOC. (b) PR. (c) VM-DPC.

PR become out of control, and the powers start to oscillate after the parameters change. The frequencies of the main oscillation components of the S-VOC and PR control are about 56 and 51 Hz, which are consistent with the analytical results as presented in Fig. 15. The VSC using the VM-DPC control remains stable. Therefore, the accuracy of the admittance model and correctness of the Nyquist stability criterion are confirmed.

Finally, the pros and cons of VOC, PR, and VM-DPC are summarized as presented in Table II. The results prove that the VM-DPC exhibits satisfactory control performance at the same level as VOC and PR and shows the best grid-connection stability among the three control methods.

C. Experimental Verification

The transient response characteristics of the three control strategies at the same current loop bandwidth are also tested by using an experimental prototype as presented in Fig. 19. A three-phase 7.5 kW Danfoss converter with *L*-filter is connected

to the grid. A grid simulator is used to generate 220 V rms voltage. A constant dc voltage is supplied using a dc power supply. The PCC line-to-line voltages and the currents are measured by using a DS2004A/D board. The three different control strategies are implemented by using the dSPACE DS1007 system. The parameters of the system and controllers are chosen to be the same as presented in Table I. The inner loop control parameters are set to ($\omega_{\rm n} = 408$ and $\zeta = 2.47$). Fig. 20 shows the transient response of the three different methods when the reference of active power steps from 0 to 3 kW. Note that three controllers have the same power convergence time of about 1.5 ms. The results confirm the previous analysis that three different control methods have the same transient dynamic characteristics.

VI. Conclusion

In this article, a uniformed comparative admittance analysis of grid-connected inverters using three symmetrical control strategies, i.e., S-VOC, PR control, and VM-DPC, is presented. The control methods are uniformed by the same power tracking dynamic expressed by a second-order transfer function. The admittance models of the three control methods considering voltage filtering and feedforward linearization are derived based on an unified framework, and the adverse effect of the different symmetrical controllers on the system harmonic response is compared by using virtual admittance. The simulation and experimental results show that the transient response of three methods are the same. The admittance analysis presents the difference in the admittance characteristics mainly reflect near the fundamental frequency. The grid-connected VSC using VM-DPC seems to be the least sensitive toward voltage harmonics. Moreover, it also exhibits the highest stability among the three symmetrical controllers. The bode plots of the equivalent admittances of the VSC using S-VOC and PR are very close to each other. The Nyquist stability criterion based on the proposed admittance modeling is verified by using the RTLAB simulation platform from Opal-RT.

Acknowledgment

The authors would like to thank Dr. C. Wu of Aalborg University, Aalborg, Denmark, for the experimental tests.

References

[1] F. Blaabjerg, Y. Yang, D. Yang, and X. Wang, "Distributed power-generation systems and protection," *Proc. IEEE*, vol. 105, no. 7, pp. 1311–1331, Jul. 2017.

[2] L. Harnefors, "Modeling of three-phase dynamic systems using complex transfer functions and transfer matrices," *IEEE Trans. Ind. Electron.*, vol. 54, no. 4, pp. 2239–2248, Aug. 2007.

[3] L. Harnefors, M. Bongiorno, and S. Lundberg, "Input-admittance calculation and shaping for controlled voltage-source converters," *IEEE Trans. Ind. Electron.*, vol. 54, no. 6, pp. 3323–3334, Dec. 2007.

[4] J. Sun, "Impedance-based stability criterion for grid-connected inverters," *IEEE Trans. Power Electron.*, vol. 26, no. 11, pp. 3075–3078, Nov. 2011.

[5] M. Cespedes and J. Sun, "Impedance modeling and analysis of grid-connected voltage-source converters," *IEEE Trans. Power Electron.*, vol. 29, no. 3, pp. 1254–1261, Mar. 2014.

[6] B. Wen, D. Boroyevich, R. Burgos, P. Mattavelli, and Z. Shen, "Analysis of D-Q small-signal impedance of grid-tied inverters," *IEEE Trans. Power Electron.*, vol. 31, no. 1, pp. 675–687, Jan. 2016.

[7] X. Wang, L. Harnefors, and F. Blaabjerg, "Unified impedance model of grid-connected voltage-source converters," *IEEE Trans. Power Electron.*, vol. 33, no. 2, pp. 1775–1787, Feb. 2018.

[8] D. Yang, X. Wang, F. Liu, K. Xin, Y. Liu, and F. Blaabjerg, "Symmetrical PLL for SISO impedance modeling and enhanced stability in weak grids," *IEEE Trans. Power Electron.*, vol. 35, no. 2, pp. 1473–1483, Feb. 2020.

[9] Mahidin, Erdiwansyah, H. Husin, Nasaruddin, M. Zaki, and Muhibbuddin, "A critical review of the integration of renewable energy sources with various technologies," *Protection Control Modern Power Syst.*, vol. 6, no. 1, pp. 1–18, 2021.

[10] Q. Liu, T. Caldognetto, and S. Buso, "Review and comparison of grid-tied inverter controllers in microgrids," *IEEE Trans. Power Electron.*, vol. 35, no. 7, pp. 7624–7639, Jul. 2020.

[11] M. Amin and M. Molinas, "Understanding the origin of oscillatory phenomena observed between wind farms and HVdc systems," *IEEE J. Emerg. Sel. Topics Power Electron.*, vol. 5, no. 1, pp. 378–392, Mar. 2017.

[12] A. Rygg, M. Molinas, Z. Chen, and X. Cai, "A modified sequence domain impedance definition and its equivalence to the dq-domain impedance definition for the stability analysis of AC power electronic systems," *IEEE J. Emerg. Sel. Topics Power Electron.*, vol. 4, no. 4, pp. 1383–1396, Dec. 2016.

[13] Y. Zhang, J. Liu, H. Yang, and J. Gao, "Direct power control of pulsewidth modulated rectifiers without DC voltage oscillations under unbalanced grid conditions," *IEEE Trans. Ind. Electron.*, vol. 65, no. 10, pp. 7900–7910, Oct. 2018.

[14] Z. Miao, "Impedance-model-based SSR analysis for type 3 wind generator and series-compensated network," *IEEE Trans. Energy Convers.*, vol. 27, no. 4, pp. 984–991, Dec. 2012.

[15] K. Sun, W. Yao, J. Fang, X. Ai, J. Wen, and S. Cheng, "Impedance modeling and stability analysis of grid-connected DFIG-based wind farm with a VSC-HVDC," *IEEE Trans. Emerg. Sel. Topics Power Electron.*, vol. 8, no. 2, pp. 1375–1390, Jun. 2020.

[16] H. Nian, B. Hu, Y. Xu, C. Wu, L. Chen, and F. Blaabjerg, "Analysis and reshaping on impedance characteristic of DFIG system based on symmetrical PLL," *IEEE Trans. Power Electron.*, vol. 35, no. 11, pp. 11720–11730, Nov. 2020.

[17] S. Fukuda and T. Yoda, "A novel current-tracking method for active filters based on a sinusoidal internal model [for PWM invertors]," *IEEE Trans. Ind. Appl.*, vol. 37, no. 3, pp. 888–895, May/Jun. 2001.

[18] S. Li, X. Wang, Z. Yao, T. Li, and Z. Peng, "Circulating current suppressing strategy for MMC-HVDC based on nonideal proportional resonant controllers under unbalanced grid conditions," *IEEE Trans. Power Electron.*, vol. 30, no. 1, pp. 387–397, Jan. 2015.

[19] R. A. Fantino, C. A. Busada, and J. A. Solsona, "Optimum PR control applied to LCL filters with low resonance frequency," *IEEE Trans. Power Electron.*, vol. 33, no. 1, pp. 793–801, Jan. 2018.

[20] Y. Liao and X. Wang, "Stationary-frame complex-valued frequency-domain modeling of three-phase power converters," *IEEE J. Emerg. Sel. Topics Power Electron.*, vol. 8, no. 2, pp. 1922–1933, Jun. 2020.

[21] B. Xie *et al.*, "Analysis and improved design of phase compensated proportional resonant controllers for grid-connected inverters in weak grid," *IEEE Trans. Energy Convers.*, vol. 35, no. 3, pp. 1453–1464, Sep. 2020.

[22] L. Harnefors, X. Wang, A. G. Yepes, and F. Blaabjerg, "Passivity-based stability assessment of grid-connected VSCs–An overview," *IEEE J. Emerg. Sel. Topics Power Electron.*, vol. 4, no. 1, pp. 116–125, Mar. 2016.

[23] P. Antoniewicz and M. P. Kazmierkowski, "Virtual-flux-based predictive direct power control of AC/DC converters with online inductance estimation," *IEEE Trans. Ind. Electron.*, vol. 55, no. 12, pp. 4381–4390, Dec. 2008.

[24] J. Hu, L. Shang, Y. He, and Z. Q. Zhu, "Direct active and reactive power regulation of grid-connected DC/AC converters using sliding mode control approach," *IEEE Trans. Power Electron.*, vol. 26, no. 1, pp. 210–222, Jan. 2011.

[25] Y. Gui, X. Wang, F. Blaabjerg, and D. Pan, "Control of grid-connected voltage-source converters: The relationship between direct-power control and vector-current control," *IEEE Ind. Electron. Mag.*, vol. 13, no. 2, pp. 31–40, Jun. 2019.

[26] Y. Gui, F. Blaabjerg, X. Wang, J. Bendtsen, D. Yang, and J. Stoustrup, "Improved DC-link voltage regulation strategy for grid-connected converters," *IEEE Trans. Ind. Electron.*, vol. 68, no. 6, pp. 4977–4987, Jun. 2021.

[27] S. Mensou, A. Essadki, T. Nasser, and B. B. Idrissi, "A direct power control of a DFIG based-WECS during symmetrical voltage dips," *Protection Control Modern Power Syst.*, vol. 5, no. 1, pp. 1–12, 2020.

[28] S. Gao, H. Zhao, Y. Gui, D. Zhou, and F. Blaabjerg, "An improved direct power control for doubly fed induction generator," *IEEE Trans. Power Electron.*, vol. 36, no. 4, pp. 4672–4685, Apr. 2021.
[29] S. Gao, H. Zhao, Y. Gui, D. Zhou, V. Terzija, and F. Blaabjerg, "A novel direct power control for DFIG with parallel compensator under unbalanced grid condition," *IEEE Trans. Ind. Electron.*, vol. 68, no. 10, pp. 9607–9618, Oct. 2021.
[30] S. Gao, H. Zhao, Y. Gui, J. Luo, and F. Blaabjerg, "Impedance analysis of voltage source converter using direct power control," *IEEE Trans. Energy Convers.*, vol. 36, no. 2, pp. 831–840, Jun. 2021.
[31] Y. Gui, M. Li, J. Lu, S. Golestan, J. M. Guerrero, and J. C. Vasquez, "A voltage modulated DPC approach for three-phase PWM rectifier," *IEEE Trans. Ind. Electron.*, vol. 65, no. 10, pp. 7612–7619, Oct. 2018.

Shuning Gao (Student Member, IEEE) received the B.S. degree in electrical engineering from the Huazhong University of Science and Technology, Wuhan, China, in 2015. He is currently working toward the Ph.D. degree with Shandong University, Jinan, China.

In 2019, he was a Visiting Student with Automation and Control Section, Department of Electronic Systems, Aalborg University, Aalborg,

Denmark. His research interests include modeling and control of power electronics and stability analysis of power electronics based power systems.

Haoran Zhao (Senior Member, IEEE) received the B.E. degree from Shandong University, Jinan, China, in 2005, the M.E. degree from the Technical University of Berlin, Berlin, Germany, in 2009, and the Ph.D. degree from the Technical University of Denmark, Kongens Lyngby, Denmark, in 2014.

He is currently a Professor with the School of Electrical Engineering, Shandong University. He was an Electrical Engineer with the State Grid Corporation of China (SGCC), Beijing, China, in 2005. From 2010 to 2011, he worked as an Application Developer with DIgSILENT GmbH, Gomaringen, Germany. His research interests include modeling and integration study of wind power, control of energy storage system, and integrated energy systems.

Peng Wang (Member, IEEE) received the M.E. degree from Shandong University, Jinan, China, in 2014, and the Dr.Ing. (*summa cum laude*) degree from the Technical University of Berlin, Berlin, Germany, in 2020.

He is currently with the School of Electrical Engineering, Shandong University. He was an Electrical Engineer with the State Grid Corporation of China (SGCC), Beijing, China, in 2018. His current research interests include modeling and stability analysis of ac–dc power system integrated with renewable generation.

Yonghao Gui (Senior Member, IEEE) received the B.S. degree in automation from Northeastern University, Shenyang, China, in 2009, and the M.S. and Ph.D. degrees in electrical engineering from Hanyang University, Seoul, South Korea, in 2012 and 2017, respectively.

From 2017 to 2018, he was with the Department of Energy Technology, Aalborg University, Aalborg, Denmark, as a Postdoctoral Researcher. Since 2018, he has been with Automation and Control Section, Department of Electronic Systems, Aalborg University, where he is currently an Assistant Professor. His research interests include control of power electronics in power systems, energy Internet, and smart grids.

Dr. Gui has served as an Associate Editor for the IEEE TRANSACTIONS ON ENERGY CONVERSION, *IEEE Power Engineering Letter*, *IEEE Access*, and *International Journal of Control, Automation, and Systems (IJCAS)*. He was a recipient of the IEEE Power and Energy Society General Meeting Best Conference Paper Award in 2019 and the IJCAS Academic Activity Award in 2019.

Vladimir Terzija (Fellow, IEEE) was born in Donji Baraci (former Yugoslavia). He received the Dipl-Ing., M.Sc., and Ph.D. degrees in electrical engineering from the University of Belgrade, Belgrade, Serbia, in 1988, 1993, and 1997, respectively.

He has been the Engineering and Physical Science Research Council (EPSRC) Chair Professor of power system engineering with the School of Electrical and Electronic Engineering, The University of Manchester, Manchester, U.K., since 2006. From 1997 to 1999, he was an Assistant Professor with the University of Belgrade, Belgrade, Serbia. From 2000 to 2006, he was a Senior Specialist for switchgear and distribution automation with ABB, Ratingen, Germany. His current research interests include smart grid applications; wide-area monitoring, protection, and control; multienergy systems; switchgear and transient processes; ICT, data analytics, and digital signal processing applications in power systems.

Dr. Terzija is the Editor-in-Chief for the *International Journal of Electrical Power and Energy Systems*, Alexander von Humboldt Fellow, as well as a DAAD and Taishan Scholar. He was the recipient of the National Friendship Award, China, in 2019. Since 2018, he has been the National Thousand Talents Distinguished Professor with Shandong University, Jinan, China.

Frede Blaabjerg (Fellow, IEEE) received the Ph.D. degree in electrical engineering from Aalborg University, Aalborg, Denmark, in 1995.

He was with ABB-Scandia, Randers, Denmark, from 1987 to 1988. He became an Assistant Professor in 1992, an Associate Professor in 1996, and a Full Professor of power electronics and drives in 1998. In 2017, he became a Villum Investigator. He is Honoris Causa with University Politehnica Timisoara (UPT), Timisoara, Romania, and Tallinn Technical University (TTU), Tallinn, Estonia. His current research interests include power electronics and its applications such as in wind turbines, PV systems, reliability, harmonics, and adjustable speed drives. He has authored or coauthored more than 600 journal papers in the fields of power electronics and its applications. He is the coauthor of four monographs and editor of ten books in power electronics and its applications.

Dr. Blaabjerg is the recipient of 33 IEEE Prize Paper Awards, the IEEE PELS Distinguished Service Award in 2009, the EPE-PEMC Council Award in 2010, the IEEE William E. Newell Power Electronics Award in 2014, the Villum Kann Rasmussen Research Award in 2014, the Global Energy Prize in 2019, and the 2020 IEEE Edison Medal. He was the Editor-in-Chief for the IEEE TRANSACTIONS ON POWER ELECTRONICS from 2006 to 2012. He was the Distinguished Lecturer for the IEEE Power Electronics Society from 2005 to 2007 and for the IEEE Industry Applications Society from 2010 to 2011 as well as from 2017 to 2018. From 2019 to 2020, he served as the President of IEEE Power Electronics Society. He has been the Vice-President of the Danish Academy of Technical Sciences. He is nominated in 2014–2020 by Thomson Reuters to be among the most 250 cited researchers in engineering in the world.